POLITECNICO
MILANO 1863

SCUOLA DI INGEGNERIA INDUSTRIALE
E DELL'INFORMAZIONE

# Station keeping of Halo orbits at the Sun-Earth and Earth-Moon $L_2$: failure analysis with the Floquet mode approach

Tesi di Laurea Magistrale in
Space Engineering - Ingegneria Spaziale

Author: **Davide Intravaia**

Student ID: 965583
Advisor: Prof. Camilla Colombo
Co-advisors: Elisa Maria Alessi, Mathilda Bolis
Academic Year: 2022-23

# Abstract

Halo orbits represent orbital trajectories located around Lagrange points within the framework of the Circular Restricted Three Body Problem dynamics (CR3BP). In this thesis, Halo orbits around the $L_2$ Lagrange point, within both the Sun-(Earth+Moon) and Earth-Moon systems, are considered. Given the inherent instability of the $L_2$ Lagrange point, it becomes imperative to implement an effective station keeping strategy. This research aims to achieve this goal by implementing and thoroughly investigating the Floquet Mode Approach (FMA) as a control algorithm. The core of this study is dedicated to conducting a failure analysis of the FMA employing a Monte Carlo simulation. This analysis aims to uncover boundaries and critical factors that influence the effectiveness of the FMA in control Halo orbits, thereby contributing to a deeper understanding of its practical applicability. Within the established operational limits, this study includes two distinct applications. The first application concerns the Radiation Environment Monitor for Energetic Cosmic rays (REMEC) mission. In this case, a preliminary analysis is conducted to assess station keeping costs. The second application involves the Bi-Circular Restricted Four Body Problem (BR4BP), where the algorithm's utility is explored in a different dynamical model.

**Keywords:** Halo orbit, Floquet Mode Approach, Monte Carlo simulation, failure analyses, Earth-Moon system, Sun-Earth system

# Sommario

Le orbite Halo rappresentano traiettorie orbitali situate attorno ai punti di Lagrange nel contesto del Problema dei Tre Corpi Ristretto e Circolare (CR3BP). In questa tesi, vengono esaminate le orbite Halo attorno al punto di Lagrange $L_2$, sia nel sistema Sole-(Terra+Luna) che nel sistema Terra-Luna. Data l'innata instabilità del punto di Lagrange $L_2$, diventa essenziale implementare una strategia di mantenimento della stazione efficace. Questa tesi si prefigge di raggiungere questo obiettivo attraverso l'implementazione e l'indagine approfondita del Floquet Mode Approach (FMA) come algoritmo di controllo. Il nucleo di questo studio è dedicato all'esecuzione di un'indagine delle cause di fallimento del FMA mediante una simulazione di Monte Carlo. Questa analisi mira a scoprire i limiti e i fattori critici che influenzano l'efficacia del FMA nel controllo delle orbite Halo, contribuendo così a una comprensione più approfondita della sua applicabilità pratica. All'interno dei limiti operativi stabiliti, questo studio comprende due diverse applicazioni. La prima applicazione riguarda la missione Radiation Environment Monitor for Energetic Cosmic rays (REMEC). In questo caso, viene condotta un'analisi preliminare per valutare i costi di mantenimento della stazione. La seconda applicazione coinvolge il Problema dei Quattro Corpi Ristretto e Circolare (BR4BP), in cui viene esplorata l'utilità dell'algoritmo in un diverso sistema dinamico.

**Parole chiave:** orbite Halo, Floquet Mode Approach, simulazione di Monte Carlo, analisi dei fallimenti, sistema Sole-Terra, sistema Terra-Luna

# Acknowledgements

Vorrei prima di tutto ringraziare la Prof. Camilla Colombo per avermi dato l'opportunità di svolgere questa tesi, e per il continuo supporto e pazienza che ha avuto nel rispondere ai miei dubbi e perplessità.
Un grazie anche ad Elisa e Mathilda per le numerose indicazioni e suggerimenti nel portare avanti e concludere questa tesi.

# Contents

# Nomenclature

**Acronyms**

2BP Two Body Problem

3BP Three Body Problem

AU Astronomical Unit

CM Center of Mass

CNSA China National Space Administration

CR3BP Restricted Three Body Problem

CSA Canadian Space Agency

EM Earth-Moon

ESA Europe Space Agency

FMA Floquet Mode Approach

ISEE-3 International Sun Earth Explorer-3

NASA National Aeronautics and Space Administration

ODE Ordinary Differential Equations

R2BP Restricted Two Body Problem

R3BP Restricted Three Body Problem

REMEC Radiation Environment Monitor for Energetic Cosmic rays

s/c spaceraft

SE Sun-Earth

SMD Space Manifolds Dynamics

SRP Solar Radiation Pressure

| | |
|---|---|
| STM | State Transition Matrix |
| ZVCs | Zero Velocity Curves |

**Variables and Constants**

| | | |
|---|---|---|
| $\boldsymbol{\Phi}$ | State transition matrix | - |
| $\boldsymbol{\rho}$ | Dimensionless position vector in rotating frame | - |
| $\boldsymbol{\varphi}$ | Flow of the system | - |
| $\boldsymbol{I}$ | Moments of inertia | $kgm^2$ |
| $\boldsymbol{M}$ | Monodromy matrix | - |
| $\boldsymbol{R}$ | Position vector in inertial frame | $km$ |
| $\boldsymbol{r}$ | Position vector in rotating frame | $km$ |
| $\mu$ | Mass parameter | - |
| $\omega_i$ | Poincarè exponents | - |
| $G$ | Gravitational constant | $\frac{m^3}{kgs^2}$ |
| $J$ | Jacobi constant | - |
| $k$ | Stability index | - |
| $L_{1,2,3}$ | Collinear Lagrange points | - |
| $L_{4,4}$ | Equilateral Lagrange points | - |
| $m$ | mass | kg |
| $m_i$ | Monodromy matrix eigenvalues | - |
| $n$ | Mean motion | $\frac{rad}{s}$ |
| $P_{AU}$ | Radiation pressure at 1AU | $\frac{N}{m^2}$ |
| $P_{AU}$ | Radiation pressure at s/c distance | $\frac{N}{m^2}$ |
| $T$ | Orbital period | s |
| $T_{gg-max}$ | Maximum torque due to Gravity gradient | Nm |
| $T_{mag-max}$ | Maximum torque due to Earth's magnetic field | Nm |
| $T_{srp-max}$ | Maximum torque due to SRP | Nm |

| | |
|---|---|
| $V$ | Total potential - |
| $V_{x,y,z}$ | Total potential partial derivatives - |
| $V_{xx,yy,zz}$ | Total potential double partial derivatives - |
| $[\hat{\boldsymbol{i}}, \hat{\boldsymbol{j}}, \hat{\boldsymbol{k}}]$ | General versors - |
| $[\hat{\boldsymbol{X}}, \hat{\boldsymbol{Y}}, \hat{\boldsymbol{Z}}]$ | Inertial reference frame - |
| $[\boldsymbol{x}, \boldsymbol{y}, \boldsymbol{z}]$ | Rotating reference frame - |

# List of Figures

# List of Tables

# 1 | Introduction

In astrodynamics celestial bodies motions, both natural and artificial, are governed by the mutual gravitational influence. Space mission design exploits different dynamical models, defined by the number of bodies considered.

The most popular and simplest one is the Two Body Problem (2BP), where two objects, with mass $m_1$ and $m_2$, influence each other with their mutual gravitational force. An assumption can be done, if $m_2 << m_1$, the object with mass $m_2$ is considered under the only gravitational influence of the other object with mass $m_1$. The resulting dynamics is called Restricted Two Body Problem (R2BP) and Kepler's laws are obtained. In all those cases where a central body is present (e.g Earth) the dynamics of a second body (e.g spacecraft (s/c)) can be approximated through the Kepler's laws. The patch conic method exploits the 2BP to design interplanetary space missions, in particular all those with high energy trajectories.

Since the R2BP doesn't cover all the characteristics of the space environment, more precise and complete models were sought, such as the Space Manifolds Dynamics (SMD). The latter exploits the natural dynamics of the solar system and it improves the mission design in terms of accuracy and cost, resulting in a more suitable and realistic model for the development of low-energy trajectories [4].

In this case the simplest dynamical model is called Three Body Problem (3BP), where a third body has been added with respect to the 2BP. Also in this model is possible to assume that $m_2 << m_1$ and $m_2 << m_3$, thus $m_2$ is considered under the only gravitational influence of the others two bodies. The resulting dynamics is called Restricted Three Body Problem (R3BP).

A slightly different model can be developed by introducing an additional assumption: if the motion of $m_1$ and $m_3$ occurs on a circular orbit*, the model is called Circular Restricted Three Body Problem (CR3BP).

In the environment of the CR3BP five equilibrium points exist. They are called Lagrangian points and in the last decades they have been exploited in many space mission applications. Their importance is growing in time since they maintain a fixed configuration

*This assumption is valid if the orbital motion has a small eccentricity

and they are suitable for different space mission scenarios, from deep space observation to Sun observations.
This thesis has been developed in the field of the CR3BP, with an application in a Bi-Circular Restricted Four Body problem (BR4BP). The BR4BP with respect to the CR3BP adds a further celestial body. Furthermore, it is called Bi-Circular because the third massive body rotates around one of the two primaries (e.g Moon around the Earth).

## 1.1. Motivation and goals

The Lagrangian points are divided in equilateral Lagrange points $L_{4,5}$ and collinear Lagrange points $L_{1,2,3}$, Fig. 1.1. The $L_{1,2}$ points are the most exploited as space missions' operational locations, but they are unstable, thus an object does not naturally orbit in their vicinity without a proper control system on-board.
Adequate station maintenance is required on the operational orbit to ensure the proper development and conclusion of the mission.
Starting from the mission ISEE-3, launched in 1978, numerous methods to control a spacecraft around Lagrange points have been developed. It's important to understand how a control system works, in order to comprehend its limits and behaviours in different mission scenarios, such that a space mission in this environment can be designed in the best way.
In a mission scenario at Lagrange points, especially at $L_2$, there are three main drivers that characterize the mission design: the s/c shall communicate with the Earth avoiding eclipses, it shall be visible to the Sun for the solar panels and the maneuver insertion cost should be as low as possible. These three drivers can be achieved with high amplitude orbits [32]. Therefore, in this thesis, a station keeping algorithm will be thoroughly tested and studied for both low and high amplitude orbits.

In literature, there are some comparisons between different control methods as [11, 19, 33]. However, these studies compared algorithm for specific mission orbits.
In [6], a Monte Carlo simulation was performed at the Sun-Earth, Earth-Moon and in high fidelity model for multiple L2 Halo orbits. The primary objective of that research is to examine various control strategies utilizing the Floquet Mode Approach, specifically for those orbits where the algorithm works.
The objective of this thesis is to push the algorithm beyond its limits, examining its behavior as it approaches failure and the reasons behind it, with the aim of gaining a clearer understanding of the algorithm's operational boundaries.

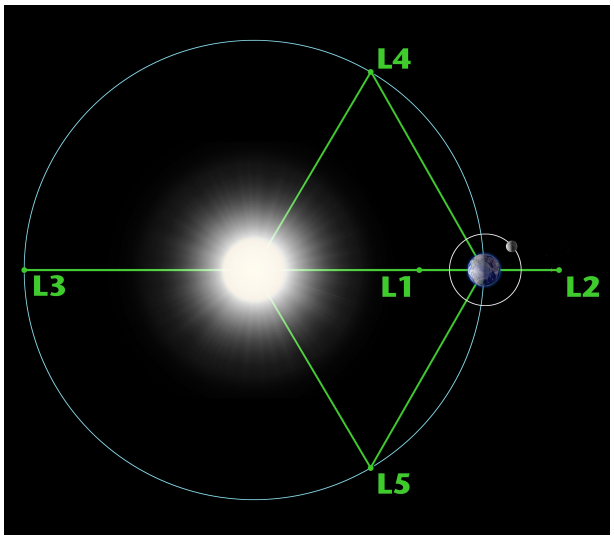


Figure 1.1: Sun-Earth system Lagrange points, not in scale. [23]

## 1.2. Thesis structure

The structure of the thesis is the following: in Chapter 2 the literature review about CR3BP and station keeping methods is going to be presented. In Chapter 3 the dynamics models is going to be shown, about CR3BP, halo family in L2 and BR4BP. In Chapter 4, the Floquèt Mode Approach (FMA) controller is going to be developed; As in Chapter 5, a simulation of the station keeping algorithm in Sun-(Erth+Moon) and Earth-Moon systems is proposed and the algorithm limitations are going to be presented. In Chapter 6, two applications of the station keeping algorithm are considered: one in Sun-(Earth+Moon) system at $L_2$, for the baseline option of Radiation Environment Monitor for Energetic Cosmic rays (REMEC) mission [1]. For the former case, also major perturbations along all mission phases will be defined [36], and the other one in BR4BP environment. In Chapter 7 conclusions and future works are presented.

# 2 | Literature research

## 2.1. Circular Restricted Three Body Problem

As previously mentioned, the space environment has to be modelled to design a space mission in the correct way. For our purpose the CR3BP has been implemented.
The first studies 3BP were made by Newton in Philosophiae Naturalis Principia Mathematica (1687). Since 3BP has no a closed solution, Euler began to study a simplified version of the problem and in 1767 he formulated CR3BP in a rotating synodic reference frame, in which the two main mass bodies are on the same axis rotating on the same barycenter. At the same time Lagrange found two solutions of the problem in which the masses move aligned or at the vertex of an equilateral triangle, and the Lagrange points were found, where the gravitational forces are in equilibrium.
Another important characteristic of the CR3BP is the Jacobi integral, discovered by Jacobi in 1836. The Jacobi integral is a constant of motion. It was used by Hill in 1877 to define and important tool: the Zero Velocity Curves (ZVCs). The ZVCs give insights about the motion of the s/c, showing regions where the s/c is allowed to move.
Thereafter, Poincaré used the Hill's studies to find the first periodic orbits.
Over the centuries, CR3BP has been studied to the present day. The CR3BP was studied in depth by Szebehely in 1967 [35], giving an important reference to study orbit families around Lagrange points.

### 2.1.1. Linear dynamics

Linear dynamics of periodic orbits around equilibrium points has been studied to understand the nonlinear behavior of these dynamical systems, in particular around $L_1$ and $L_2$. The result is that the linear dynamics is of the type center x center x saddle [32]. The saddle indicates hyperbolic behavior, one stable and the other unstable. Therefore, the problem will have two eigenvalues (stable and unstable) and two eigenvectors, respectively. The eigenvectors represent two directions in which the s/c can be perturbed: in one case it will converge, in the other it will diverge from the periodic orbit. These

manifolds can be used to bring the s/c from Earth to Lagrange points and vice-versa. This hyperbolic behaviour makes $L_{1,2}$ very unstable thus a station keeping technique is required for the design of orbits around them.

### 2.1.2. Orbits around Lagrange points

The computation of periodic orbits around Lagrange points is challenging due to hyperbolic behaviour of the CR3BP. The goal is to eliminate the hyperbolic parts since from the center manifold is possible to obtain two families called Lyapunov orbits (vertical and horizontal), shown in Fig. 2.1.

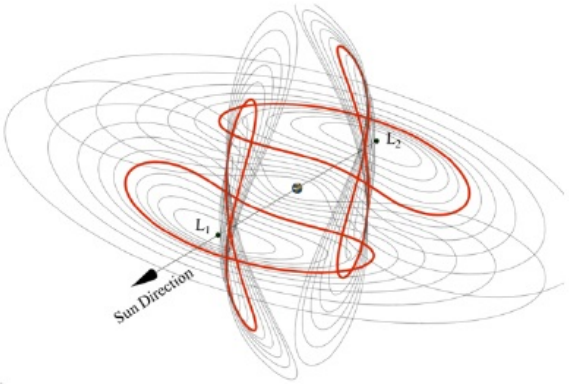


Figure 2.1: Horizontal and vertical Lyapunov family [38].

From literature there are three ways to compute only the center manifold, thus the periodic orbits: reduction method [18], a semi-analytical approach which exploits the Poincaré–Lindstedt method [27] and numerical methods as in [20, 32, 39]. In this thesis the a numerical method based on the Newton's method has been implemented.
In addition to Lyapunov orbits, there are also 2-D quasi-periodic orbits called Lissajous orbits Fig. 2.2 that connect the two families of Lyapunov orbits. A specific solution of the Lissajous orbits are the well-known Halo orbits. The Halo orbits can be computed analytically, considering the in-plane and out-of-plane frequencies to be equal [10]. Halo orbits are 3-D periodic orbits, symmetric with respect to $x$-$z$ plane. In this thesis, Halo orbits in the Sun-(Earth+Moon) and Earth-Moon reference frame will be studied.

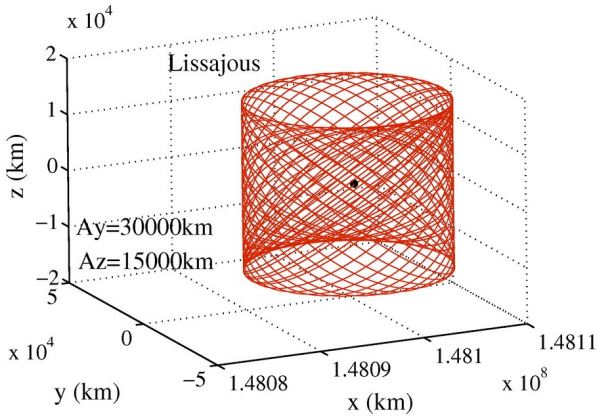


Figure 2.2: Lissajous family [26].

The computation of the periodic orbits around Lagrange points is strongly depending on the mass parameter $\mu$. A complete classification can be found on Soldini's Ph.D. theses [32].

### 2.1.3. Space missions at Lagrange points

This section will list the main space missions to $L_2$ in the Sun-(Earth + Moon) and Earth-Moon systems. The main data were taken from [30]. Since this thesis focuses on the development of a station keeping algorithm, station keeping costs will be reported where they could be found.
Table 2.1 shows how the station keeping costs per year in $L_2$ is generally in the order of m/s. Thus the cost is not so high, however, an adequate station strategy must be developed for mission success.

## 2.2. Station keeping: state of the art

This section provides a brief discussion and list of the main station-keeping strategies.
The classification of station keeping methods is carried out as following [30]. A first classification is done if the algorithm is based on *Dynamical effects* and it will be classified as (CAT.i) while the other are based on the *General control theory* (CAT.ii). Within both categories, two kind of control strategies exist: *Impulsive*(A) and *Continuous*(B). Moreover these methods are suitable for either linear or non-linear dynamics.

[†]Sun-Earth.
[†]Earth-Moon.

| **Missions** | **Agency** | **Launch date** | **Status** | **Orbits** | **System** | $\boldsymbol{A_z}[km]$ | $\boldsymbol{\Delta V}[m/s/y]$ |
|---|---|---|---|---|---|---|---|
| WMAP | NASA | 2001 | conluded | Lissajous | SE* | $264{\cdot}10^3$ | 1.2 |
| Herschel | ESA/NASA | 2009 | conluded | Halo | SE | $400{\cdot}10^3$ | 1 |
| Planck | ESA | 2009 | conluded | Lissajous | SE | $300{\cdot}10^3$ | 1 |
| Chang'e 2 | CNSA | 2011 | conluded | Lissajous | SE | $400{\cdot}10^3$ | - |
| Euclid | ESA | 2023 | current | Halo | SE | $100{\cdot}10^3$ | 2 |
| JWST | NASA/ESA/CSA | 2021 | current | Lissajous | SE | $418 \cdot 10^3$ [25] | 2 [7] |
| Gaia | ESA | 2013 | current | Lissajous | SE | $100{\cdot}10^3$ | 2 |
| ARTEMIS P1 | NASA | 2013 | concluded | Quasi-halo | EM† | $35.30{\cdot}10^3$ | 7.39 |
| Chang'e 5-T1 | CNSA | 2013 | concluded | Lissajous | EM | $35{\cdot}10^3$ | - |

Table 2.1: Successful missions in $L_2$ .

The well-known method within the *CAT.i.A* is *Floquét mode approach* (linear), developed by Simò et al. [31] and later, in 2001 Gòmez et al. [12], which exploits the *Floquét modes*. In *CAT.i.B* are included *Hamiltonian structure preserving* (linear) developed by Scheers et al. in 2003[28], which stabilizes the orbit in the sense of Lyapunov stability and the *Pole placement technique* (linear) developed by Gurfil at al. in 2006 [15].
In *CAT.ii.A* there are *Target point technique* (linear) developed by Howell et al. in 1993 [17], which can be a very flexible method and the *Sliding mode control*(non-linear) developed by Shahid et al. in 2010 [29].
In *CAT.ii.B* are included *Linear feedback control* developed in 1970 by Farquhar [9] and in 1973 by Breakwell [2] the *$\theta$-D method* (non-linear) developed by Xin et al. in 2008 [37]. Some of these methods have been implemented exploiting the *Solar radiation pressure* (SRP) to control the orbit (e.g. HSP integrating with SRP [33]).
Linear methods and methods belonging to *CAT.i* used especially to understand as best as possible the dynamics of the problem and are methods exploiting the dynamics of the problem itself. Developing these methods provide very useful and qualitative information about the problem which has been studied [19]. Therefore, *Floquét mode approach* method have been selected and implemented in this thesis.

# 3 | Dynamic models

This chapter will present the main dynamic models used in the thesis, their development and their main characteristics.

## 3.1. Circular Restricted Three Body Problem

As already mentioned in Chapter 1, CR3BP derives from some assumptions of the *n-body* problem. The first assumption is the number of bodies considered. It's obvious as in our case the number of body, which we will identify as n, is n = 3. Fig. 3.1 shows a graphical representation of the model considered.

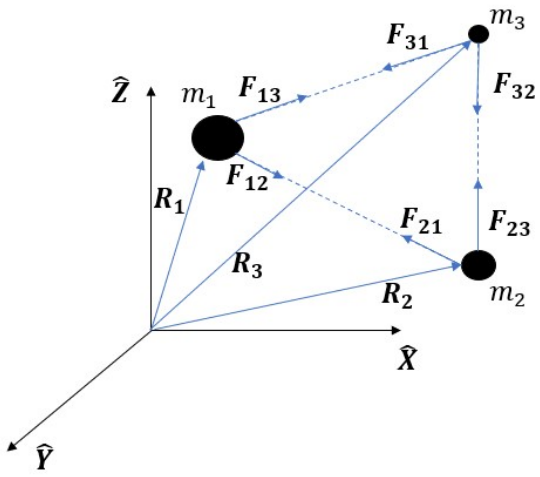


Figure 3.1: 3BP representation in inertial frame.

The three bodies are governed by Newton's law of universal gravitation:

$$F = G\frac{m_1 m_2}{d^2} \tag{3.1}$$

Where $m_1$ and $m_2$ are the two primaries' masses, $d$ is the norm of their distance, $G$ the universal gravitational constant and $F$ the gravitational force. Therefore, applying the

second Newton's law, the equations of motion of the overall system in the inertial frame can be retrieved Eq. (3.2):

$$\begin{cases} m_1\ddot{\boldsymbol{R}}_{\boldsymbol{1}} = G\dfrac{m_1 m_2}{R_{12}^3}\boldsymbol{R_{12}} + G\dfrac{m_1 m_3}{R_{13}^3}\boldsymbol{R_{13}}, \\ m_2\ddot{\boldsymbol{R}}_{\boldsymbol{2}} = G\dfrac{m_2 m_1}{R_{21}^3}\boldsymbol{R_{21}} + G\dfrac{m_2 m_3}{R_{23}^3}\boldsymbol{R_{23}}, \\ m_3\ddot{\boldsymbol{R}}_{\boldsymbol{3}} = G\dfrac{m_3 m_1}{R_{31}^3}\boldsymbol{R_{31}} + G\dfrac{m_3 m_2}{R_{32}^3}\boldsymbol{R_{32}}. \end{cases} \tag{3.2}$$

A further assumptions can be done, if $m_3 << m_1$ and $m_3 << m_2$, we can state that $m_3$ does not influence the other two bodies thus $m_1$ and $m_2$ will move following the second Kepler's law. Moreover, in some particular cases, the motion of the two primaries ($m_1$, $m_2$) can be assumed to be circular.
In this thesis the two primaries are defined by the system Sun-(Earth+Moon), where the Sun and the Earth+Moon system revolve around their common center of mass in a circular motion. The plane on which the primaries move is the ecliptic, and the third body is represented by the s/c.
Before deriving the equations of motion is important to define two reference frames one inertial and the other rotating.

### 3.1.1. Reference frames

The CR3BP is defined in a rotating frame $(\boldsymbol{x}, \boldsymbol{y}, \boldsymbol{z})$ with respect to an inertial frame$(\hat{\boldsymbol{X}}, \hat{\boldsymbol{Y}}, \hat{\boldsymbol{Z}})$. Fig.3.2 shows the two reference systems that have the same origin that coincides with the system Sun-(Earth+Moon)'s center of mass (CM); The two primaries both lie on the $\boldsymbol{x}$ axis; $\boldsymbol{z}$ is the rotation axes and coincides with $\hat{\boldsymbol{Z}}$; The rotating frame rotates on the ecliptic plane with a constant mean motion $n^*$; at t=0 the two reference frames will coincide.

*Mean motion $n = \sqrt{\dfrac{2\pi}{T}}$ where T is the period of the rotating frame

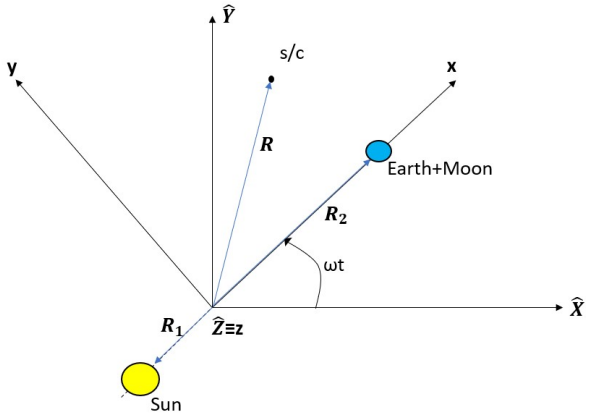


Figure 3.2: Inertial and rotating reference frames representation.

With these new assumptions the motion of a s/c in an inertial frame under the gravitational influence of the two primaries will be:

$$\ddot{\boldsymbol{R}} = G\frac{m_1}{|\,\boldsymbol{R_1}-\boldsymbol{R}\,|^3}(\boldsymbol{R_1}-\boldsymbol{R}) + G\frac{m_2}{|\,\boldsymbol{R_2}-\boldsymbol{R}\,|^3}(\boldsymbol{R_2}-\boldsymbol{R}) \tag{3.3}$$

Since in the next chapters the problem will be treated in the rotating frame, it is important to identify a rotation matrix that will allow to pass from a reference frame to another. Let's first define the state of the spacecraft in the inertial frame as $\boldsymbol{X} = (\boldsymbol{R}, \dot{\boldsymbol{R}})$ and the one in the rotating frame as $\boldsymbol{x}_d = (\boldsymbol{r}_d, \dot{\boldsymbol{r}}_d)^{\dagger}$. The relations to pass between the two reference systems are:

$$\begin{cases} \boldsymbol{r}_d = \mathcal{T}_{ri}\boldsymbol{R}, \\ \dot{\boldsymbol{r}}_d = \dot{\mathcal{T}}_{ri}\boldsymbol{R} + \mathcal{T}_{ri}\dot{\boldsymbol{R}}, \\ \\ \boldsymbol{R} = \mathcal{T}_{ri}^T\boldsymbol{r}_d, \\ \dot{\boldsymbol{R}} = \dot{\mathcal{T}}_{ri}^T\boldsymbol{r}_d + \mathcal{T}_{ri}^T\dot{\boldsymbol{r}}_d. \end{cases} \tag{3.4}$$

Using as reference Fig. 3.2, the direction cosine matrix $\mathcal{T}_{ri}(t)$ that appears in Eq. (3.4) can be define as:

† $\square_d$ denotes variables with dimension in the rotating frame, the absence of the subscript on the same variable indicates that the same variable is dimensionless

$$\mathcal{T}_{ri}(t) = \begin{bmatrix} \cos nt & \sin nt & 0 \\ -\sin nt & \cos nt & 0 \\ 0 & 0 & 1 \end{bmatrix} \tag{3.5}$$

A complete development of Eq. (3.4) can be found in Soldini [32].

### 3.1.2. Equations of Motion in the rotating frame

In this section, the equations of motion in the rotating reference frame are calculated and adimensionalized ([5, 20]).
Let's first define some parameters, the distance between the two primaries $l = 1AU = 1.496 \cdot 10^8 km$ and the total mass of the system:

$$M = m_1 + m_2 \quad \text{where} \quad m_1 = m_{Sun} \quad \text{and} \quad m_2 = m_{Earth} + m_{Moon} \tag{3.6}$$

Then the mass ratios are defined as:

$$\mu_1 = \frac{m_1}{M} \quad \text{and} \quad \mu_2 = \frac{m_2}{M} \tag{3.7}$$

Thanks Eq. (3.7) and Eq. (3.6) the following equation holds:

$$\mu_1 + \mu_2 = 1 \tag{3.8}$$

Defining the mass parameter $\mu = \mu_2$ and using Eq. (3.8), Eq. (3.7) becomes:

$$\mu_1 = 1 - \mu \quad \text{and} \quad \mu_2 = \mu \tag{3.9}$$

Thus the masses of the system can be expressed as function of the total mass $M$:

$$m_1 = (1 - \mu)M \quad \text{and} \quad m_2 = \mu M \tag{3.10}$$

In the same way, the distance of the primaries with respect to the CM can be expressed using the same procedure:

$$d_{d1} = \mu l \quad \text{and} \quad d_{d2} = (1 - \mu)l \tag{3.11}$$

A representation of these quantities is shown Fig. 3.3.

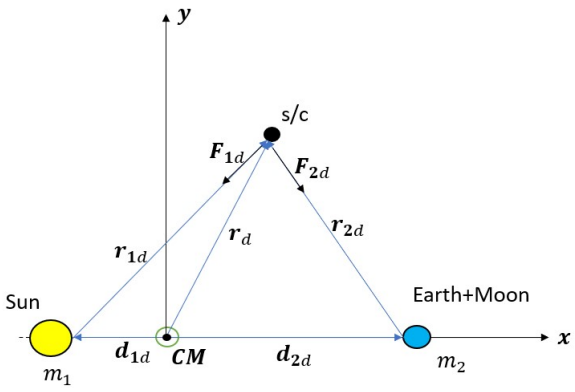


Figure 3.3: Rotating reference frame representation.

Applying Newton's second law, the vectorial formulation of the CR3BP can be expressed as:

$$\ddot{\boldsymbol{r}}_d + 2\boldsymbol{\omega} \times \dot{\boldsymbol{r}}_d + \boldsymbol{\omega} \times (\boldsymbol{\omega} \times \boldsymbol{r}_d) = \frac{1}{m}(\boldsymbol{F}_{\mathbf{1}d} + \boldsymbol{F}_{\mathbf{2}d}) = -G\frac{m_1}{r_{1d}^3}\boldsymbol{r}_{\mathbf{1}d} - G\frac{m_2}{r_{2d}^3}\boldsymbol{r}_{\mathbf{2}d} \tag{3.12}$$

Where,

- $\boldsymbol{\omega}$ : reference system angular velocity.
- $m$ : spacecraft mass.
- $\ddot{\boldsymbol{r}}_d$ : relative acceleration.
- $2\boldsymbol{\omega} \times \dot{\boldsymbol{r}}_d$ : Coriolis acceleration..
- $\boldsymbol{r}_d \times (\boldsymbol{\omega} \times \boldsymbol{r}_d)$ : centripetal acceleration.
- $\boldsymbol{r}_{\mathbf{1}d} = (x_d + \mu l)\hat{\boldsymbol{i}} + y_d\hat{\boldsymbol{j}} + z_d\hat{\boldsymbol{k}}$.
- $\boldsymbol{r}_{\mathbf{2}d} = (x_d - (1-\mu)l)\hat{\boldsymbol{i}} + y_d\hat{\boldsymbol{j}} + z_d\hat{\boldsymbol{k}}$.

By performing the vector products and substituting Eq. (3.10) and Eq. (3.11) into Eq. (3.12), the latter can be rewritten as:

$$\begin{cases} \ddot{x}_d - 2n\dot{y}_d - n^2 x_d = -GM\left[\dfrac{1-\mu}{r_{1d}^3}(x_d + \mu l) + \dfrac{\mu}{r_{2d}^3}(x_d - (1-1\mu)l)\right], \\ \ddot{y}_d + 2n\dot{x}_d - n^2 y_d = -GM\left[\dfrac{1-\mu}{r_{1d}^3}y_d + \dfrac{\mu}{r_{2d}^3}y_d\right], \\ \ddot{z}_d = -GM\left[\dfrac{1-\mu}{r_{1d}^3}z_d + \dfrac{\mu}{r_{2d}^3}z_d\right]. \end{cases} \tag{3.13}$$

The complete procedure to obtain Eq. (3.13) can be found in Appendix A.1.
Tab. 3.1 shows the parameters used to adimensionalize Eq. (3.13)

| $\mathbf{l}$ [km] | $\boldsymbol{\tau}$[s] | $\mathbf{v}$ $[km\ s^{-1}]$ |
|---|---|---|
| 1AU | $\sqrt{\frac{l^3}{GM}}$ | $\sqrt{\frac{GM}{l}}$ |

Table 3.1: Parameters to adimensionalize distance, time and velocity.

The dimensionless time parameter is $\tau = nt$, in this way the first and second time derivatives can be computed as:

$$\begin{cases} (\dot{\square}) = \dfrac{d(\square)}{dt} = n\dfrac{(\square)}{d\tau} = n(\square)' \\ \\ (\ddot{\square}) = \dfrac{d^2(\square)}{dt^2} = n^2\dfrac{(\square)}{d\tau} = n^2(\square)''. \end{cases} \tag{3.14}$$

Thus, the dimensionless equations of motion in CR3BP are:

$$\begin{cases} x'' - 2y' - x = -\dfrac{1-\mu}{r_1^3}(x+\mu) - \dfrac{x+\mu-1}{r_2^3}\mu, \\ y'' + 2x' - y = -\dfrac{1-\mu}{r_1^3}y - \dfrac{\mu}{r_2^3}y, \\ z'' = -\dfrac{1-\mu}{r_1^3}z - \dfrac{\mu}{r_2^3}z. \end{cases} \tag{3.15}$$

Where,

- $x = \dfrac{x_d}{l}$, $y = \dfrac{y_d}{l}$ and $z = \dfrac{z_d}{l}$.
- $r_1 = \sqrt{(x+\mu)^2 + y^2 + z^2}$ and $r_2 = \sqrt{(x+\mu-1)^2 + y^2 + z^2}$.

The complete procedure to obtain Eq. (3.15) is described in Appendix A.2.

Since the total potential of the system can be written as:

$$V = \underbrace{\frac{1}{2}(x^2+y^2)}_{\text{rotational}} + \underbrace{\frac{1-\mu}{r_1} + \frac{\mu}{r_2}}_{gravitational} \tag{3.16}$$

Eq. (3.15) can be rewritten to highlight the first partial derivatives of the total potential

as:

$$\begin{cases} x'' - 2y' = V_x, \\ y'' + 2x' = V_y, \\ z'' = V_z. \end{cases} \tag{3.17}$$

Where the partial derivatives $V_x$, $V_y$ and $V_z$ are

- $V_x = x - \dfrac{1-\mu}{r_1^3}(x+\mu) - \dfrac{x+\mu-1}{r_2^3}\mu$
- $V_y = y - \dfrac{1-\mu}{r_1^3}y - \dfrac{\mu}{r_2^3}y$
- $V_z = -\dfrac{1-\mu}{r_1^3}z - \dfrac{\mu}{r_2^3}z$

The total potential of the system in a rotating reference frame is composed by a rotational and gravitational contributions. Writing the equations of motion in dimensionless form highlight their only dependence on the mass parameter $\mu$.

### 3.1.3. Lagrange points

In this section the equilibrium points (Lagrange points) of the system are numerically computed using the built-in Matlab® function *fzero* ([5, 20]). To study static equilibrium the following relations have to hold:

$$x'' = y'' = z'' = x' = y' = z' = 0 \tag{3.18}$$

So:

$$\begin{cases} V_x = x - \dfrac{1-\mu}{r_1^3}(x+\mu) - \dfrac{x+\mu-1}{r_2^3}\mu & = 0, \\ V_y = y - \dfrac{1-\mu}{r_1^3}y - \dfrac{\mu}{r_2^3}y & = 0, \\ V_z = -\dfrac{1-\mu}{r_1^3}z - \dfrac{\mu}{r_2^3}z & = 0. \end{cases} \tag{3.19}$$

There are five equilibrium points: $L_{1,2,3}$ are identified as the collinear ones and $L_{4,5}$ as the equilateral Lagrange points.
As shown in Fig. 3.4, collinear equilibrium points lie on the $\boldsymbol{x}$ axis, this imply that $z = 0$ and $y = 0$. Thus, the condition to find $L_{1,2,3}$ can be recovered by Eq. (3.19):

$$V_x(x,0,0) = x - \frac{1-\mu}{(x+\mu)^2}\frac{\mu}{(x+\mu-1)^2} = 0 \tag{3.20}$$

Moreover, Fig. 3.4 shows the positions of $L_{1,2,3}$ with respect to the primaries, thus, those positions can be approximated with Eq. (3.21), then Eq. (3.20) has to be solved numerically, using the approximated values as initial conditions.

$$\begin{cases} x_{L1} = 1 - \mu - \epsilon_1, \\ x_{L2} = 1 - \mu + \epsilon_2, \\ x_{L3} = -\mu - \epsilon_3. \end{cases} \tag{3.21}$$

Where $\epsilon_1 > 0$, $\epsilon_2 > 0$ and $\epsilon_3 > 0$ are quantities to set arbitrarily, such that $x_{L1}$, $x_{L2}$ and $x_{L3}$ are close to the real ones. Since Eq. (3.19) has to hold, the choice of $\epsilon_1 > 0$ and $\epsilon_2 > 0$ can be made graphically thanks to Fig. 3.5a, while for $\epsilon_3 > 0$ thanks to Fig. 3.5b.

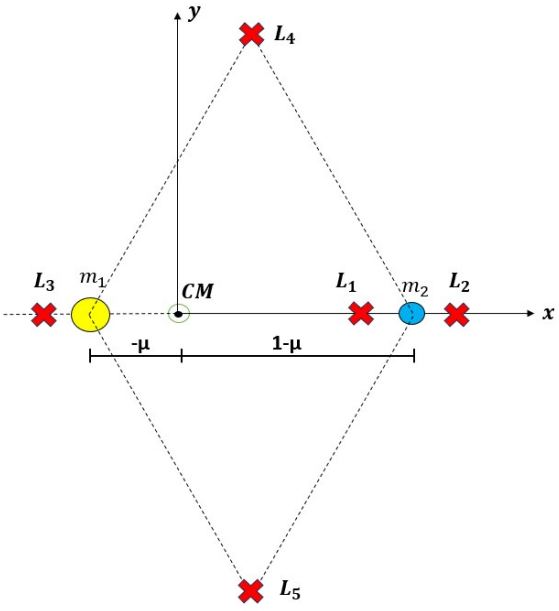


Figure 3.4: Lagrange points schematic representation.

For what concern equilateral Lagrange points, they are located on the vertices of an equilateral triangle [20], this imply that $r_1 = r_2 = 1$. Thus, $L_{4,5}$ have been calculated through geometric considerations.

The computation of Lagrange points has been performed considering the Sun-(Earth+Moon) system, with a mass parameter $\mu = 3.04042 \cdot 10^{-6}$ [34]. The results are presented in Table 3.2.

| | x [ndu] | y[ndu] | z[ndu] | x [km] | y[km] | z[km] |
|---|---|---|---|---|---|---|
| $L_1$ | 0.98998 | 0 | 0 | $1.48099 \cdot 10^8$ | 0 | 0 |
| $L_2$ | 1.01007 | 0 | 0 | $1.51105 \cdot 10^8$ | 0 | 0 |
| $L_3$ | -1 | 0 | 0 | $-1.49597 \cdot 10^8$ | 0 | 0 |
| $L_4$ | 0.49999 | 0.86602 | 0 | $7.47984 \cdot 10^7$ | $1.29555 \cdot 10^8$ | 0 |
| $L_5$ | 0.49999 | -0.86602 | 0 | $7.47984 \cdot 10^7$ | $-1.29555 \cdot 10^8$ | 0 |

Table 3.2: Lagrange points coordinates in rotating reference frame of Sun-(Earth+Moon) system

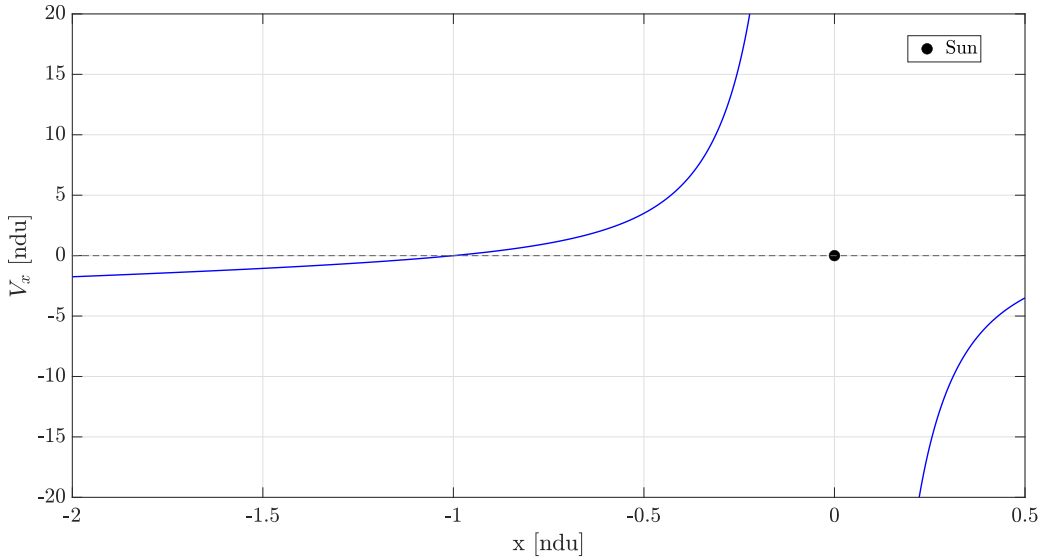


(a) Total potential derivative with respect to x around the Sun

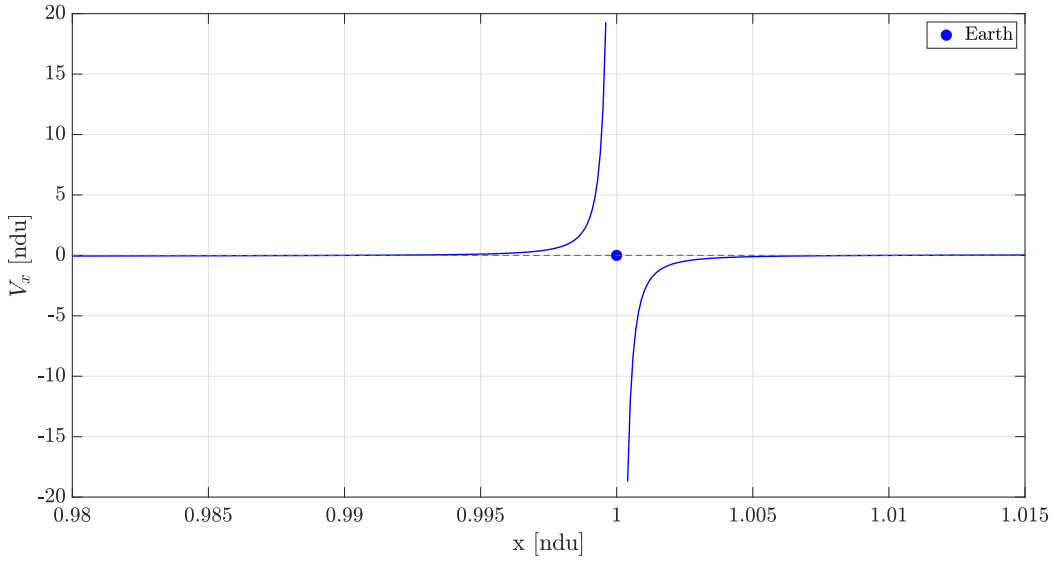


(b) Total potential derivative with respect to x around the Earth

Figure 3.5: Total potential derivative with respect to x.

### 3.1.4. Jacobi Integral and Zero Velocity Curves

The dimensionless equations of motion in CR3BP are an autonomous system, since the independent variable is time, it is called time-invariant system. A property that characterise that kind of systems are the presence of an integral of motion, a quantity that is conserved during the motion.
In the case of the CR3BP the integral of motion is called Jacobi Integral (C) [5, 20, 32]. Taking Eq. (3.17) and multiplying the first equation by $\dot{x}$, the second one by $\dot{y}$ and the third one by $\dot{z}$ and then summing the three equations,it is possible to obtain the energy derivative indicated as Eq. (3.22).

$$E' = x'x'' + y'y'' + z'z'' - 2y'x' + 2x'y' - x'V_x - y'V_y - z'V_z = 0 \tag{3.22}$$

Eq. 3.22 is easily integrable, the Jacobi Integral is obtained:

$$E = \frac{1}{2}\frac{dv^2}{d\tau} - \frac{dV}{d\tau} = \frac{d}{d\tau}(v^2 - 2V) = 0 \Longrightarrow (v^2 - 2V) = -C = const \tag{3.23}$$

Where $v^2 = x'^2 + y'^2 + z'^2$. The equation can be rewritten knowing that $V = -U$, where U is the total potential energy.
In Chapter 2, it was indicated how the Jacobi integral was exploited by Hill to obtain insights about the motion of a s/c around Lagrange points. Some conclusions can be retrieved from Eq. (3.23):

- $2V - C > 0 \Longrightarrow v^2 > 0$ : possible motion.
- $2V - C < 0 \Longrightarrow v^2 < 0$ : impossible motion

This means that there are areas where $v^2 = 0$ and $C^* = 2V$. $C^*$ is called Critical Jacobi constant. It defines limits between possible motion (allowed regions) and impossible motion (forbidden regions), these boundary surfaces are called Zero velocity curves (ZVCs).

An example of ZVCs, for the Earth-Moon system, is reported in Fig. 3.6. It is evident how a s/c needs to increase its energy to enlarge its possible motion. What has just been said is made more evident by Fig. 3.7. The figure shows that for some levels of energy the s/c is literally bounded around one of the two masses (Case 1); if the energy increases the motion between the two masses becomes possible (Case 2). As the energy increases further, the motion becomes larger and larger (Case 3-4), until the s/c can move freely (Case 5).

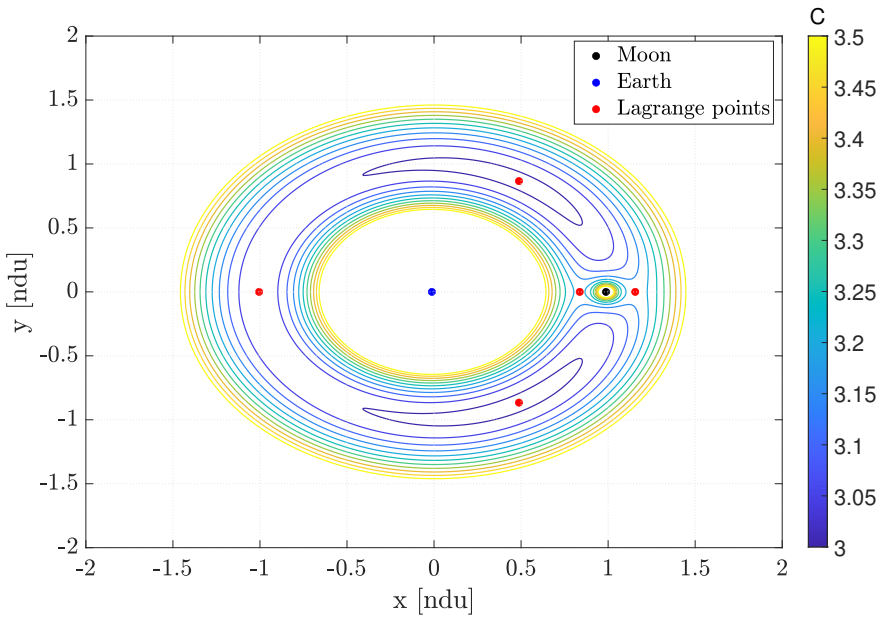


Figure 3.6: Zero velocity curves for Earth-Moon system, with $\mu = 0.0121505$.

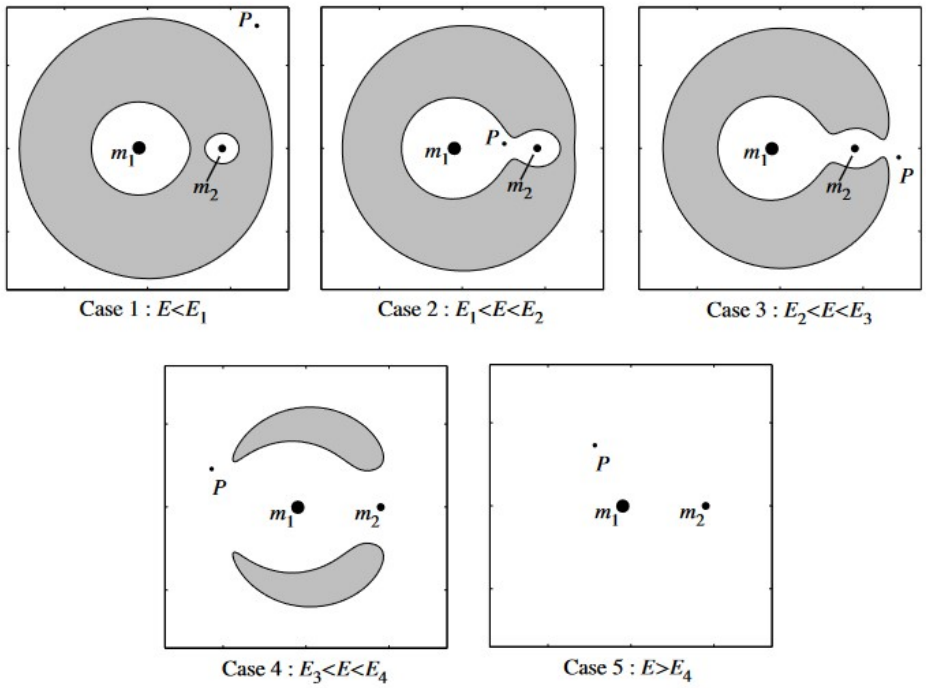


Figure 3.7: Areas in which the spacecraft can travel according to its energy level [20].

### 3.1.5. Linearised equations of motion

As far as, we know that the collinear Lagrange points are unstable, while the equilateral Lagrange points are stable, to be able to affirm this, it is necessary to study the local

stability of the system. The equation of motions Eq. (3.15) must be linearised in the vicinity of each Lagrange point, such that the eigenvalues of the linearised equations can be computed in order to study the stability of the system.
If $x_{eq}$, $y_{eq}$ and $y_{eq}$ are the components of the position of a generic Lagrange point, it is necessary to perturb them such that:

$$\begin{cases} x = x_{eq} + \xi, \\ y = y_{eq} + \eta, \\ z = z_{eq} + \zeta. \end{cases} \Longrightarrow \begin{cases} x' = x'_{eq}, \\ y' = y'_{eq}, \\ z' = z'_{eq}. \end{cases} \tag{3.24}$$

Then, a Taylor expansion can be developed for the left hand side of Eq. (3.15), evaluating it at the equilibrium points and neglecting higher-order terms:

$$\begin{cases} \dfrac{\partial V}{\partial x}(x,y,z) = \cancelto{0}{\dfrac{\partial V}{\partial x}\bigg|_{eq}} + \dfrac{\partial^2 V}{\partial x^2}\bigg|_{eq} \xi + \dfrac{\partial^2 V}{\partial y \partial x}\bigg|_{eq} \eta + \dfrac{\partial^2 V}{\partial z \partial x}\bigg|_{eq} \zeta, \\ \dfrac{\partial V}{\partial y}(x,y,z) = \cancelto{0}{\dfrac{\partial V}{\partial y}\bigg|_{eq}} + \dfrac{\partial^2 V}{\partial y^2}\bigg|_{eq} \eta + \dfrac{\partial^2 V}{\partial x \partial y}\bigg|_{eq} \xi + \dfrac{\partial^2 V}{\partial z \partial y}\bigg|_{eq} \zeta, \\ \dfrac{\partial V}{\partial z}(x,y,z) = \cancelto{0}{\dfrac{\partial V}{\partial z}\bigg|_{eq}} + \dfrac{\partial^2 V}{\partial z^2}\bigg|_{eq} \zeta + \dfrac{\partial^2 V}{\partial x \partial z}\bigg|_{eq} \xi + \dfrac{\partial^2 V}{\partial y \partial z}\bigg|_{eq} \eta. \end{cases} \tag{3.25}$$

Knowing Eq. (3.15), Eq. (3.24), and Eq. (3.25), the linearised equations of motion are:

$$\begin{cases} \xi'' - 2\eta' = V_{xx}^{eq}\, \xi + V_{xy}^{eq}\, \eta + V_{xz}^{eq}\, \zeta, \\ \eta'' + 2\xi' = V_{yy}^{eq}\, \eta + V_{yx}^{eq}\, \xi + V_{yz}^{eq}\, \zeta, \\ \zeta'' = V_{zz}^{eq}\, \zeta + V_{zx}^{eq}\, \xi + V_{zy}^{eq}\, \eta. \end{cases} \tag{3.26}$$

Equation (3.26) can be written in vectorial form:

$$\frac{d}{d\tau}\begin{bmatrix}\xi\\ \eta\\ \zeta\\ \xi'\\ \eta'\\ \zeta'\end{bmatrix} = \begin{bmatrix}0 & 0 & 0 & 1 & 0 & 0\\ 0 & 0 & 0 & 0 & 1 & 0\\ 0 & 0 & 0 & 0 & 0 & 1\\ V_{xx}^{eq} & V_{xy}^{eq} & V_{xz}^{eq} & 0 & 2 & 0\\ V_{yx}^{eq} & V_{yy}^{eq} & V_{yz}^{eq} & -2 & 0 & 0\\ V_{zx}^{eq} & V_{zy}^{eq} & V_{zz}^{eq} & 0 & 0 & 0\end{bmatrix} \Longrightarrow \boldsymbol{X'} = \boldsymbol{AX} \tag{3.27}$$

Where the matrix $\boldsymbol{A}$ is composed as:

$$\boldsymbol{A} = \begin{bmatrix}\boldsymbol{0} & \boldsymbol{I}\\ \boldsymbol{V}_J & \boldsymbol{J}\end{bmatrix} \quad ; \quad \boldsymbol{J} = \begin{bmatrix}0 & 2 & 0\\ -2 & 0 & 0\\ 0 & 0 & 0\end{bmatrix} \tag{3.28}$$

The matrix $\boldsymbol{V}_J$ is the Jacobian matrix of the total potential evaluated at the equilibrium points. In Appendix A.3 the full expression of the Jacobian is presented. Now, it is possible to compute the eigenvalues of $\boldsymbol{A}$, thus the stability of Lagrange points: $L_1$, $L_2$ and $L_3$ will have a real and positive eigenvalue that determines the instability, while $L_4$ and $L_5$ will have all the eigenvalues on complex axis and negative plane that determine stability.

## 3.2. Halo orbits design

In this section, the mathematical tools used to compute the Halo family of orbits will be presented. Since the equations of motion do not have a closed solution, there are techniques that exploit geometrical characteristics of the orbit. In this thesis the numerical method known as Differential correction or Shooting method has been implemented.

### 3.2.1. State Transition Matrix

Before introducing the methodology used to compute Halo orbits, another tool have to be introduced: the State Transition Matrix (STM). The dynamics in the CR3BP can be expressed in a compact and general way as:

$$\begin{cases}\dot{\boldsymbol{x}} = f(\boldsymbol{x}, t),\\ \boldsymbol{x}(t_0) = \boldsymbol{x}_0.\end{cases} \tag{3.29}$$

where $\boldsymbol{x}_0$ is the initial value of the state. In this scenario, it possible to define a function that map the initial condition $\boldsymbol{x}_0$ at time $t$ to the final condition $\boldsymbol{x}$ at time $t$, as shown in Fig. 3.8. This function is called flow of the dynamics such that $\boldsymbol{x} = \boldsymbol{\varphi}(\boldsymbol{x}_0, t_0, t)$. Thus the flow is the system of ODEs.

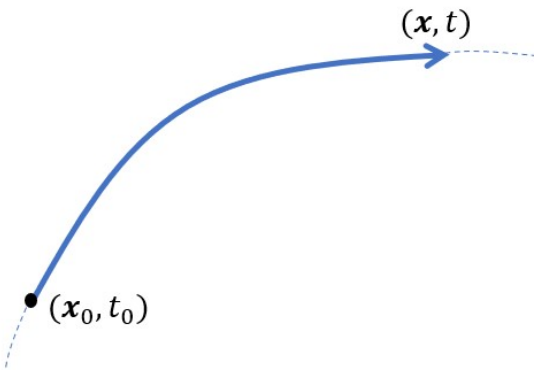


Figure 3.8: Mapping of initial conditions through flow

If we have perturbed initial conditions that are propagated through the flow Eq. (3.30). The final conditions will be displaced with respect to those not perturbed Fig. 3.9.

$$\boldsymbol{x} + \delta\boldsymbol{x} = \boldsymbol{\varphi}(\boldsymbol{x}_0 + \delta\boldsymbol{x}_0, t_0, t) \tag{3.30}$$

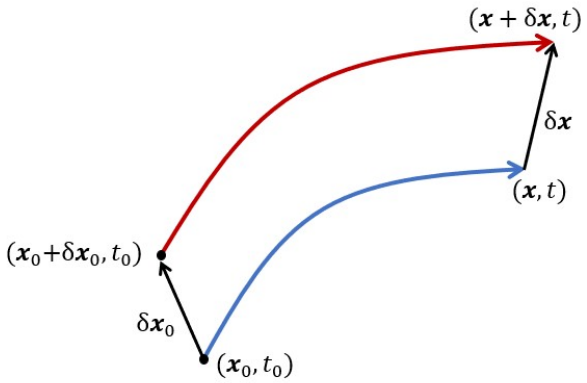


Figure 3.9: Mapping of perturbed initial conditions through flow

If the deviations with respect to the initial conditions are small, the flow can be linearised, and the following equation is obtained:

$$\delta \boldsymbol{x} = \frac{\partial \boldsymbol{\varphi}}{\partial \boldsymbol{x}_0}(\boldsymbol{x}_0, t_0, t)\delta \boldsymbol{x}_0 \Longrightarrow \delta \boldsymbol{x} = \boldsymbol{\Phi}(\boldsymbol{x}_0, t_0, t)\delta \boldsymbol{x}_0 \tag{3.31}$$

Where $\boldsymbol{\Phi}(\boldsymbol{x}_0, t_0, t)$ is the STM (Jacobian of the flow) and it is a linear analytic map between $\delta \boldsymbol{x}_0$ and $\delta \boldsymbol{x}$. The full derivation can be found in Appendix A.4.

In this thesis the STM will be computed numerically, through the use of variational equations Eq. (3.27) that can be written in the following way:

$$\delta \dot{\boldsymbol{x}}(t) = \boldsymbol{A}(t)\delta \boldsymbol{x}(t) \tag{3.32}$$

Deriving with respect to time Eq. (3.31),

$$\delta \dot{\boldsymbol{x}} = \boldsymbol{\Phi}(\boldsymbol{x}_0, t_0, t)\delta \dot{\boldsymbol{x}}_0 \tag{3.33}$$

Taking into account Eq. (3.32), Eq. (3.33) and Eq. (3.31) tthe following equation is obtained:

$$\dot{\boldsymbol{\Phi}}(\boldsymbol{x}_0, t_0, t) = \boldsymbol{A}(t)\boldsymbol{\Phi}(\boldsymbol{x}_0, t_0, t) \tag{3.34}$$

Equation (3.34) can be integrated to compute the STM at each time step, where the initial conditions will be $\boldsymbol{\Phi}(\boldsymbol{x}_0, t_0, t_0) = \mathbf{I}_6$[†]

### 3.2.2. Differential corrections

Since the mathematical problem in trajectory design is a Two boundary Value Problem type, the differential correction methods are used.
In this thesis the Multi-variable Newton method has been implemented [24, 39]. The Multi-variable Newton method is a generalization of the classical Newton's method. In this section its main features will be presented.

Let's first introduce a vector that collects all those free variables that can be modified:

$$\boldsymbol{X} = \begin{bmatrix} X_1 \\ \vdots \\ X_n \end{bmatrix} \tag{3.35}$$

[†] $\mathbf{I}_6$ is identity matrix 6x6

Where $n$ is these number of free variables. Some of free variables are constrained , thus a vector constraint can be defined:

$$\boldsymbol{F}(\boldsymbol{X}) = \begin{bmatrix} F_1(\boldsymbol{X}) \\ \vdots \\ F_m(\boldsymbol{X}) \end{bmatrix} = 0 \tag{3.36}$$

The goal is to find a vector $\boldsymbol{X}^*$ such that $F(\boldsymbol{X}^*) = 0$, which can be done using the Newton's method. In this application, since we have multiple variables, we are going to apply a Multi-variable Newton method.
Let's expand Eq. (3.36) with a Taylor expansion up to the first order:

$$\boldsymbol{F}(\boldsymbol{X}) = \boldsymbol{F}(\boldsymbol{X}_0) + \frac{\partial \boldsymbol{F}(\boldsymbol{X}_0)}{\partial \boldsymbol{X}_0}(\boldsymbol{X} - \boldsymbol{X}_0) \tag{3.37}$$

Thus, substituting Eq. (3.36) into Eq. (3.43), the following equation is obtained:

$$\boldsymbol{F}(\boldsymbol{X}_0) + D\boldsymbol{F}(\boldsymbol{X}_0)(\boldsymbol{X} - \boldsymbol{X}_0) = 0 \tag{3.38}$$

Where $D\boldsymbol{F}(\boldsymbol{X}_0)$ is the Jacobian matrix of the problem of size $m \times n$. At this point Eq. (3.38) can be written in iterative way:

$$\boldsymbol{X}^{j+1} = \boldsymbol{X}^j - D\boldsymbol{F}(\boldsymbol{X}^j)^{-1}\boldsymbol{F}(\boldsymbol{X}^j) \tag{3.39}$$

The iteration process continue up to a certain value of $\boldsymbol{X}^{j+1}$ such that $\boldsymbol{F}(\boldsymbol{X}^{j+1}) < \epsilon$, where $\epsilon$ is a selected tolerance..

### 3.2.3. Single shooting: Halo orbits

In the previous sections the STM and the Multi-variable Newton method have been presented. Now, these two tools can be joined together to implement the *Single shooting* procedure to compute Halo orbits.
Halo orbits are 3D periodic orbits, symmetric with respect $x - z$ plane. This plane is intersected perpendicularly, thus, the only component velocity on that plane is along $y$. This means that a generic initial condition on $x - z$ plane can be written as:

$$\boldsymbol{x} = [x_0 \,;0\,; z_0 \,;0\,; \dot{y}_0 \,;0] \tag{3.40}$$

The target condition is to reach after half period $(T/2)$, the same $x-z$ plane, where $y_t = 0$, $\dot{x}_t = 0$ and $\dot{z}_t = 0$[‡]. By fixing the coordinate $z_0$, the free variables vector can be defined as:

$$\boldsymbol{X}_0 = \begin{bmatrix} x_0 \\ \dot{y}_0 \\ T \end{bmatrix} \tag{3.41}$$

Knowing the symmetry conditions to impose, the constraint vector can be formulated as:

$$\boldsymbol{F}(\boldsymbol{X}_0) = \begin{bmatrix} y(T/2) - y_t \\ \dot{x}(T/2) - \dot{x}_t \\ \dot{z}(T/2) - \dot{z}_t \end{bmatrix} < \epsilon \tag{3.42}$$

At this points the Jacobian matrix of the constraints with respect to the the free variables can be computed:

$$D\boldsymbol{F}(\boldsymbol{X}_0) = \frac{\partial \boldsymbol{F}(\boldsymbol{X}_0)}{\partial \boldsymbol{X}_0} = \begin{bmatrix} \frac{\partial y}{\partial x_0} & \frac{\partial y}{\partial \dot{y}_0} & \frac{\partial y}{\partial T} \\ \frac{\partial \dot{x}}{\partial x_0} & \frac{\partial \dot{x}}{\partial \dot{y}_0} & \frac{\partial \dot{x}}{\partial T} \\ \frac{\partial \dot{z}}{\partial x_0} & \frac{\partial \dot{z}}{\partial \dot{y}_0} & \frac{\partial \dot{z}}{\partial T} \end{bmatrix} = \begin{bmatrix} \Phi_{21} & \Phi_{25} & \dot{y} \\ \Phi_{41} & \Phi_{45} & \ddot{x} \\ \Phi_{61} & \Phi_{65} & \ddot{z} \end{bmatrix} \tag{3.43}$$

Where $\Phi$ is the STM.
To conclude, the new vector of free variable is derived:

$$\boldsymbol{X} = \begin{bmatrix} x_0 \\ \dot{y}_0 \\ T \end{bmatrix} - \begin{bmatrix} \Phi_{21} & \Phi_{25} & \dot{y} \\ \Phi_{41} & \Phi_{45} & \ddot{x} \\ \Phi_{61} & \Phi_{65} & \ddot{z} \end{bmatrix} \begin{bmatrix} y(T/2) - y_t \\ \dot{x}(T/2) - \dot{x}_t \\ \dot{z}(T/2) - \dot{z}_t \end{bmatrix} \tag{3.44}$$

Then, the new initial conditions can be reformulated and the procedure is iterated from Eq. (3.41) to Eq. (3.44), until the constraint vector(Eq. (3.42)) is within the tolerance $\epsilon$.

### 3.2.4. Orbit continuation

Orbit continuation is a technique used to generate a family of orbits [14, 20]. In this thesis, it has been used to generate $L_2$ southern Halo family for Sun-(Earth+Moon) and

[‡] $\square_t$ are the target conditions

Earth-Moon systems.
Halo families can be generated from the bifurcation of a 2D Lyapunov orbit [14]. A generic initial condition for a Lyapunov orbit on the $x-z$ symmetric plane can be:

$$\boldsymbol{x}_1 = [x_0\ ;0\ ;0\ ;0\ ;\dot{y}_0\ ;0] \tag{3.45}$$

Since Halo orbits are 3D orbits, an initial condition for the first Halo orbit can be generated from Eq. (3.45), adding a perturbation (d) to the $z$ coordinate:

$$\boldsymbol{x}_1 = [x_0\ ;0\ ;d\ ;0\ ;\dot{y}_0\ ;0] = [x_0\ ;0\ ;z_1\ ;0\ ;\dot{y}_0\ ;0] \tag{3.46}$$

With this new initial condition the new orbit can be computed with the procedure shown in Section 3.2.3.
The updating procedure continue such that the initial condition for the new orbit will be:

$$\boldsymbol{x}_n = [x_{n-1}\ ;0\ ;z_{n-1}+d\ ;0\ ;\dot{y}_{n-1}\ ;0] \tag{3.47}$$

The iteration on the coordinate $z$ continue until the $z$ coordinated change more rapidly than the $x$ coordinate:

$$|x_n - x_{n-1}| < |z_n - z_{n-1}| \tag{3.48}$$

When $x$ will change more rapidly than $z$, the same iteration expressed in Eq. (3.47) can be done on $x$ coordinate.

### 3.2.5. Halo orbits stability

Halo orbits' stability has been computed with an numerical approach as in [3, 32].
Let's first define the *Monodromy matrix*[12, 19] as the STM evaluated after one Halo orbital period:

$$\boldsymbol{M} = \boldsymbol{\Phi}(\boldsymbol{x_0}, t_0, T) \tag{3.49}$$

The eigenvalues of the Monodromy matrix have the following form:

$$\begin{aligned} &m_1 > 1 \\ &m_2 = \frac{1}{m_1} < 1 \\ &m_3 = m_4 = 1 \\ &m_5 = {m_6}^* \end{aligned} \tag{3.50}$$

The eigenvalues of $\boldsymbol{M}$ provide information on the global stability of Halo orbits: if they lie outside the unit circle[§] in the complex plane, they represent instability, if they lie within it they indicate stability, and if they are equal to unity they identify marginal stability. The eigenvalues $m_1$ and $m_2$ are associated to the hyperbolic behaviour: $m_1$'s eigenvector indicates the most expanding direction, while, $m_2$'s eigenvector indicates the converging direction; $m_3 = m_4 = 1$ are associated to neutral variables, there is only one eigenvector associated to the eigenvalue equal to one and it is tangent to the orbit, the other eigenvalues is associated to a variation of a variable (e.g. energy or period) that change along the orbits family; $m_5 = m_6{}^*$ are complex conjugate pair, their modulus is equal to one and they define a rotating plane. This is due to an existence of a quasi-periodic orbit around the Halo orbit. Moreover, the computation of the *Invariant manifolds* in the CR3BP exploits the Monodromy matrix, since the Monodromy matrix gives the direction of stable and unstable direction.

Now, the stability index can be defined as:

$$k = tr(\boldsymbol{M}) - 2 \tag{3.51}$$

A Halo orbit can be defined as stable if $k$ is in the range $\pm 2$.

### 3.2.6. Halo family characteristics

In this section, it will be presented the southern $L_2$ Halo family in the Sun-(Earth-Moon) system and the major parameters that characterizing these orbits. All the tools just presented have been used to generate the family and to derive the parameters.
Figure 3.10 shows the Halo family parameterized with respect to the amplitude $A_z$[¶].

[§]the Monodromy matrix gives discrete information, thus the eigenvalues are studied with respect on the unitary circle of complex plane

[¶]$A_z$ is selected as the maximum value that the coordinate $z$ assumes.

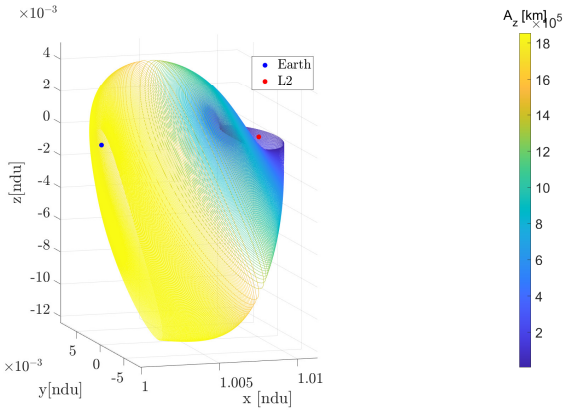


Figure 3.10: $L_2$ Sun-Earth Halo family parameterized with the amplitude.

Figure 3.10 shows how the amplitude increases as the orbit approaches the Earth, except for the orbits most closed to it, where $A_z$ begins slightly decrease.
Figure 3.11 shows how the main Halo orbit parameters change as function of $A_z$. The orbital period (Fig. 3.11a) decreases when the amplitude increases, passing from a maximum value of 180 days to a minimum of 100 days. Also the Jacobi constant (Fig. 3.11b) decrease as amplitude increases. The stability index (Fig. 3.11c) shows that the more stable orbits are those more closest to Earth. The same figure shows that in some cases the stability index is within the interval $\pm 2$, those orbits are stable and they are called *Near rectilinear Halo orbits* (NRHO). NRHO are indeed stable, and will not be considered as a case study in this thesis.

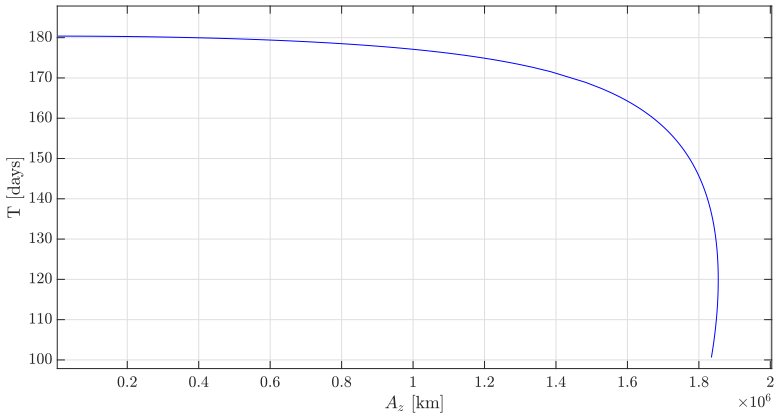


(a) Orbital period

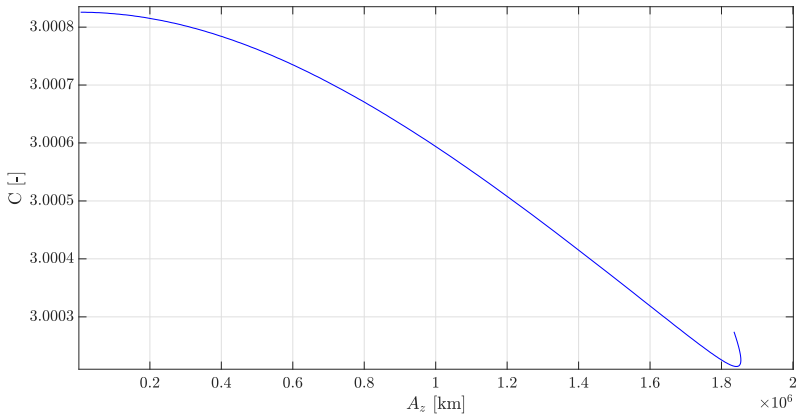


(b) Jacobi constant

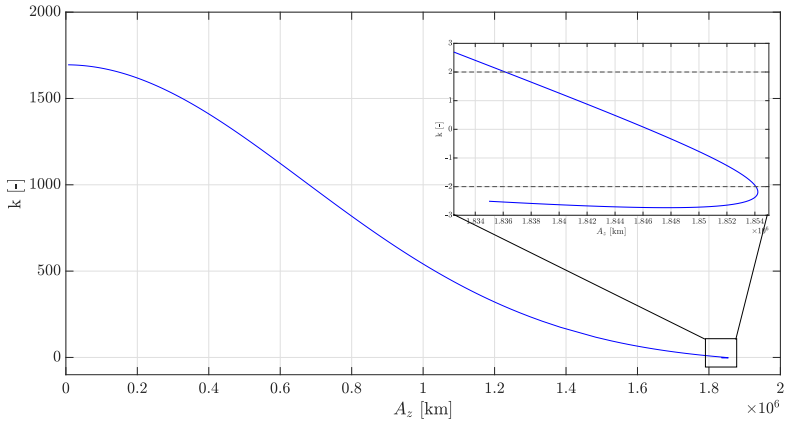


(c) Stability index

Figure 3.11: Halo family main characteristics.

## 3.3. Bi-Circular Restricted Four Body Problem

As in this thesis, an application of station keeping in the four-body environment will be presented, this section will introduce a specific dynamics, referred to as the *Bi-circular Restricted Four-Body Problem* .

The dynamics implemented was developed by [22], where the fourth body is introduced within the dynamics of the CR3BP as a perturbation. The additional body in this case will be the Moon, Fig. 3.12 shows a graphical representation of the model.

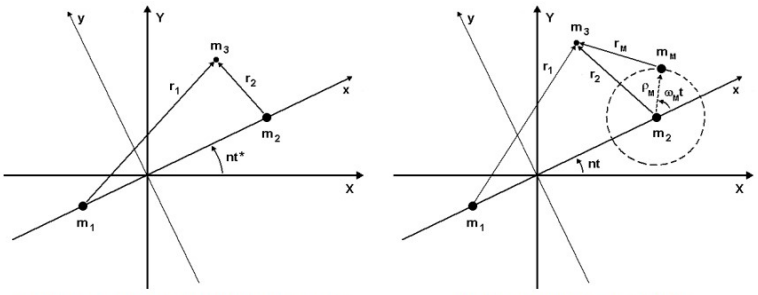


(a) Classic circular planar restricted three-body problem. (b) Moon-perturbed Sun–Earth RTBP.

Figure 3.12: CR3BP and BR4BP representation [22].

The equations of motion have the same form of Eq. (3.17), the only difference is inside the total potential $V$ that in this case takes into account the presence of the Moon:

$$V_M(x, y, z, \mu, \theta) = V(x, y, z, \mu, \theta) + \frac{m_M}{r_M} - \frac{m_M}{\rho_M^2}(x\cos\theta + y\sin\theta) \tag{3.52}$$

where,

- $\dot{\theta} = \omega_M = 1.2367 \cdot 10\ [ndu]$ : Moon's angular velocity.
- $m_M = 3.6942 \cdot 10^{-8}\ [ndu]$ : Moon's mass.
- $\rho_M = 2.5721 \cdot 10^{-3}\ [ndu]$ : Earth-Moon's distance
- $r_M^2 = (x - 1 + \mu - \rho_M\cos\theta)^2 + (y - \rho_M\sin\theta)^2$ : s/c-Moon's distance.

# 4 | Floquét Mode Approach

The FMA is a method that exploits SMD, in particular it is a control method used in CR3BP dynamics that makes use of the theory of invariant manifolds. The method, developed in [12, 31], aims to cancel the unstable component of the error state vector (e.g. with an impulsive maneuver), such that the s/c can naturally converge towards the nominal orbit. The information about stable and unstable directions are not recovered from STM, since its elements grow exponentially in time [19], but from the Floquèt modes. This Chapter presents the main components required for FMA development and shows the implementation of the algorithm.

## 4.1. Floquèt Modes

As indicated above, since Floquèt modes are periodic functions, they are used to obtain indication about the stable and unstable directions. The method used to compute the modes follows the procedure found in Keeter [19], thus the Floquèt modes can be computed numerically by this formula:

$$\tilde{\boldsymbol{E}}(t, t_0) = \boldsymbol{\Phi}(t, t_0) S e^{-\tilde{\boldsymbol{J}} t} \tag{4.1}$$

Matrix $S$ is a real matrix that collects the eigenvectors of the Monodromy matrix, Eq. (3.49). The complex eigenvectors have to be separated in imaginary and real part to keep $S$ a real matrix.
$\tilde{J}$ is a Jordan matrix that depends on the eigenvalues of the Monodromy matrix, Eq. (3.50). Let's define Poincarè exponents $\omega_i$:

- for a real eigenvalue $(m_i)$ : $\omega_i = \dfrac{1}{T} \ln m_i = r_i$.
- for a complex eigenvalue $(m_i = a_i + b_i j)$ : $\omega_i = r_i + \theta_i j$, where $r_i = \dfrac{1}{T} \ln \left(\sqrt{a_i^2 + b_i^2}\right)$ and $\theta_i = \dfrac{1}{T} \arctan\left(\dfrac{b_i}{a_i}\right)$

Thus the Jordan matrix is defined as:

$$\tilde{\boldsymbol{J}} = \begin{bmatrix} r_1 & & & & & \\ & r_2 & & & & \\ & & r_3 & & & \\ & & & r_3 & & \\ & & & & r_5 & \theta_5 \\ & & & & -\theta_5 & r_5 \end{bmatrix} \tag{4.2}$$

Due to inaccurate integration or numerical problem, it could happen that $m_3$ and $m_4$ are not a pure real number but they have a very small imaginary part, in those few cases they are treated as a complex number.

## 4.2. Controller definition: one-axis and two-axes controllers

Different controllers exist [11, 16, 19], but the aim of all of them is to eliminate the unstable component of the error state vector. The error state vector is defined as the difference between the actual spacecraft state and the nominal one. It is an error both in position and velocity, thus the FMA requires the knowledge of the entire state of the spacecraft. Let's define the error state vector:

$$\boldsymbol{\delta}(t) = [\delta x\ ; \delta y\ ; \delta z\ ; \delta \dot{x}\ ; \delta \dot{y}\ ; \delta \dot{z}] \tag{4.3}$$

The Floquèt modes (Eq. (4.1)) can be used as base to express the error state vector (Eq. (4.3)) at any time along the orbit, such that:

$$\boldsymbol{\delta}(t) = \sum_{i=1}^{6} c_i \boldsymbol{e}_i(t) \tag{4.4}$$

Where $\boldsymbol{e}_i$ are the vector components of the matrix defined in Eq. (4.1). Since $\boldsymbol{e}_1$ is the unstable direction, the aim is to cancel the component $c_1$. Before that, the projection factor $\boldsymbol{\pi}_1$ along the unstable direction has to be computed as the signed minor of the first column of the matrix $[\boldsymbol{\delta}\ , \boldsymbol{e}_2\ , \boldsymbol{e}_3\ , \boldsymbol{e}_4\ , \boldsymbol{e}_5\ , \boldsymbol{e}_6]$. At this point the unstable component can be computed projecting the error state vector along the unstable component:

$$c_1 = \boldsymbol{\pi}_1(t) \cdot \boldsymbol{\delta}(t) \tag{4.5}$$

If $\boldsymbol{\Delta}$ is the maneuver to cancel the unstable component, Eq. (4.4) becomes:

$$\begin{bmatrix} \delta x \\ \delta y \\ \delta z \\ \delta \dot{x} \\ \delta \dot{y} \\ \delta \dot{z} \end{bmatrix} + \begin{bmatrix} 0 \\ 0 \\ 0 \\ \Delta_x \\ \Delta_y \\ \Delta_z \end{bmatrix} = \boldsymbol{\delta} + \boldsymbol{\Delta} = \sum_{i=2}^{6} c_i \boldsymbol{e}_i(t) \tag{4.6}$$

This implies that:

$$\boldsymbol{\pi}_1(t) \cdot \boldsymbol{\Delta} = -c_1 = \pi_4(t)\Delta_x + \pi_5(t)\Delta_y + \pi_6(t)\Delta_z \tag{4.7}$$

Selecting $\Delta_y = 0$ and $\Delta_z = 0$, the maneuver to cancel the unstable component of the error state vector along the $x$ direction will be:

$$\Delta_x = -\frac{c_1}{\pi_4(t)} \tag{4.8}$$

In the case of the two-axis controller, it is necessary to minimize the Euclidean norm of Eq. (4.7) [16], therefore, imposing $\boldsymbol{\Delta}_z = 0$:

$$\Delta_x = -\frac{c_1 \pi_4(t)}{\pi_4^2(t) + \pi_5^2(t)} \quad ; \quad \Delta_y = -\frac{c_1 \pi_5(t)}{\pi_4^2(t) + \pi_5^2(t)} \tag{4.9}$$

In this thesis, single-axis and two-axis control has been implemented,but there are also cases in the literature where three-axis control is exploited [11, 19].

## 4.3. Real mission scenario

In order to make the simulation close to a real mission, some parameters have to be defined. This section is going to talk about *Operational errors* and *Mission constraints*.

### 4.3.1. Operational errors

All the errors will be generated with a Gaussian distribution with mean equal to zero.
In the simulation three kinds of operational errors have been introduced:

- **Orbit injection error**: the s/c shall reach its nominal orbit, but it will not be released exactly on a point belonging to it, thus it will have different nominal position

and velocity.

- **Orbit determination error**: the s/c during the operational phase of the mission shall be monitored from ground, so that its state can be determined. Again, the data acquisition will not be precise and the position and velocity states acquired will be different. This will introduce an orbit determination error.
- **Orbit maneuver errors**: the propulsion system on the s/c will be inaccurate, thus it will not provide precisely the correct maneuver. This kind of error can be of two type: an error in magnitude or in direction of the maneuver. In this thesis only the magnitude error has been modelled.

### 4.3.2. Mission constraints

Also some mission constraints are introduced to simulate a real mission scenario.

- **Minimum tracking time**: this is the minimum time between two orbit determination. It is a very specific parameter for each mission, since it depends on the mission operational orbit (e.g. eclipses) or on telecommunication constraints (e.g. antennas availability/visibility).
- **Minimum maneuver magnitude**: This constraint is important for two reasons: the former relates to the propulsion system, as an impulsive system cannot physically produce a manoeuvre below a certain value; the latter is that if the magnitude of the manoeuvre is too little, it could be of the same order of magnitude of the tracking errors [4, 19].
- **Minimum time between maneuvers**: this constraint indicates the minimum time between two successive maneuvers. This parameter is limited by the first constraint, in fact a maneuver cannot be done before an orbit determination acquisition. Moreover, it can be also a design parameter for the propulsion system since it determines the number of total firings.

## 4.4. Station keeping algorithm

In this Section, the implemented algorithm will be shown. The algorithm consists of two main parts: the former is used to selected the design parameters and to produce and store all the information necessary for the latter, which is the actual station keeping algorithm.

First of all, the operational orbit has to be selected. Then, the initial conditions are

integrated over one orbital period to obtain the nominal orbit, the STM and the Monodromy matrix. At this point the STM and the Monodormy matrix are used to compute the Floquèt modes along one orbit. Next, the nominal orbit and the Floquèt modes are interpolated and replicated for n orbital periods and they are stored. The operational errors and mission constraints can be selected. Now, the station keeping algorithm simulation can be performed.
The procedure is illustrated below with a list of steps:

- **Initialization:**

1. Select the operational orbit.
2. Integrate the initial state $\boldsymbol{x}_0$ over one orbital period to compute nominal orbit $\boldsymbol{x}_{nom}$, the state transition matrix $\boldsymbol{\Phi}$, for each state of $\boldsymbol{x}_{nom}$, and the Monodromy matrix $\boldsymbol{M}$.
3. Compute Floquèt modes $\boldsymbol{E}$ using $\boldsymbol{\Phi}$ and $\boldsymbol{M}$.
4. Define the number of orbits (n) for the simulation
5. Replicate interpolated data ($\boldsymbol{E}$, $\boldsymbol{x}_{nom}$) for n obits and store them.
6. Decide operational errors and mission constraints.
7. Perturb $\boldsymbol{x}_0$ with orbit injection errors.

- **Station keeping algorithm:**

1. Integrate up to next tracking point and obtain the real state $\boldsymbol{x}_{real}$.
2. Generate orbit determination errors $\boldsymbol{err}_{OD}$ and add it to $\boldsymbol{x}_{real}$ to compute the estimated state $\boldsymbol{x}_{estim} = \boldsymbol{x}_{real} + \boldsymbol{err}_{OD}$.
3. Compute the error state vector $\delta\boldsymbol{x} = \boldsymbol{x}_{estim} - \boldsymbol{x}_{nom}$
4. Assessment of manoeuvre (it depends on control strategy)
   (a) if no need to perform a maneuver, restart from point **1**.
   (b) if a maneuver is necessary, continue.
5. Compute projection factor along unstable direction $\boldsymbol{\pi}_1$ with $\delta\boldsymbol{x}$.
6. Compute the unstable component $c_1$
7. Compute the maneuver $\boldsymbol{\Delta}$

8. Compute magnitude orbit maneuver error $\boldsymbol{err}_{man}$ and add it to $\boldsymbol{\Delta}$ to compute the real maneuver $\tilde{\boldsymbol{\Delta}} = \boldsymbol{\Delta} + \boldsymbol{err}_{man}$.
9. Change the real state adding the maneuver $\boldsymbol{x}_{real} = \boldsymbol{x}_{real} + \tilde{\boldsymbol{\Delta}}$.
10. Restart from point **1**.

## 4.5. Monte-Carlo simulation

In the development of the station keeping algorithm, operational errors are introduced at the beginning and during the simulation. This implies a stochastic process, so all performance parameters resulting from the simulation will be stochastic in nature. For this reason a Monte-Carlo simulation with a sample size of 100 trials [13] is performed to obtain statistically reasonable data.

### 4.5.1. Analysis of failure cases

The Monte-Carlo simulation is used also to develop a parametric analysis about the success of the station-keeping algorithm. The study will test the Floquèt mode approach on two main parameters:

- the minimum time between maneuvers, as this is an important design parameter, since knowing whether a manoeuvre can be performed every 20 days or 60 days can be useful for mission design.
- the Halo family of orbits, to understand in which cases the algorithm may fail, but more importantly why.

Thus, a parametric study has been done varying these two parameters.

# 5 | Simulation

In this Chapter, all the parameters required to define the simulation, the control strategy and the results will be shown and commented. The simulation was carried out for both Sun-(Earth+Moon) and Earth-Moon systems, analysing in particular the failure cases through a Monte Carlo method.

## 5.1. Control strategy

Various control strategies can be employed, depending on the evolution of the unstable component [31], the specific position along the orbit, regular time intervals, or deviations from the nominal orbit [11]. The latter strategy has been selected, thus some boundaries and zones need to be defined:

- **Free motion**: No manoeuvres are performed within this zone, so the spacecraft moves according to its own dynamics. The zone is bounded by the *nominal orbit* and the *starting maneuvers* lines.
- **Perform maneuver**: Maneuvers can be performed within this zone if necessary. This zone is delimited by the boundaries *starting maneuvers* and *limit maneuver*.
- **Interrupt simulation**: This zone lies beyond the boundary *limit maneuver*; if the spacecraft is in this zone, the simulation is interrupted and the station keeping algorithm is considered to have failed.

Figure 5.1 shows the terminology just introduced.

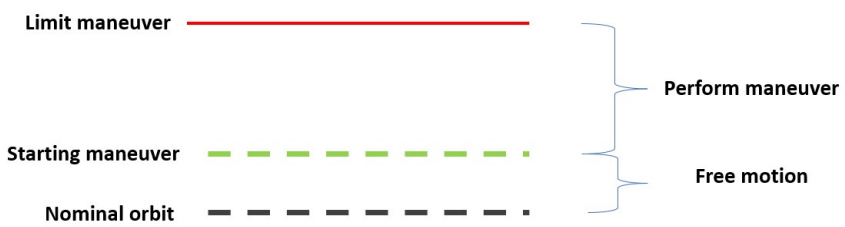


Figure 5.1: Control strategy graphical representation.

Further considerations need to be made about the *Perform maneuver* zone. A spacecraft in that zone will not always perform a maneuver, there are two cases in which the maneuver will not be done:

1. If the spacecraft is approaching the nominal orbit: followed by an OD when the actual position is closer to the nominal orbit than the previous one.
2. If the minimum time between two consecutive manoeuvres has not elapsed.

In all other cases, when the spacecraft is in that area, a maneuver will be performed.

## 5.2. Failure analysis

In this Section, as already mentioned, a failure analysis of the Floquet mode approach, applied to Halo orbits station keeping, is presented. The station keeping simulation is considered a success, if the s/c will remain within the *limit maneuver* boundary for thr prescribed simulation time. The analysis is done in the Sun-(Earth+Moon) and Earth-Moon systems.

### 5.2.1. Sun-Earth systems

Let's first analyze the station keeping in the Sun-(Earth+Moon) system. Some Halo orbits along the family have been selected, as reported in Table 5.1. Figure 5.2 graphically shows the chosen samples. The reason why these orbits were selected is that, prior to the Monte Carlo simulation, the FMA was tested along the entire Halo orbit family.It was noticed that the algorithm began to fail when a certain amplitude value was exceeded, so more orbits were selected after that value, to better analyze this behaviour.

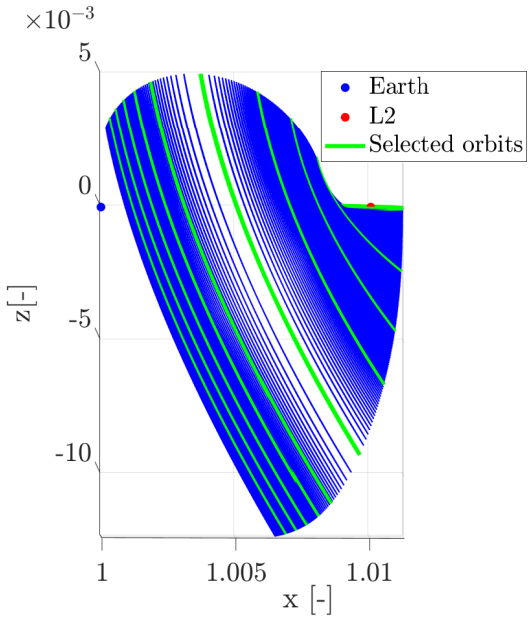


Figure 5.2: Sun-Earth systems selected orbits graphical representation.

| $A_z$ [km] | T [days] | k |
|---|---|---|
| $6.27 \cdot 10^3$ | 180.38 | 1695 |
| $3.62 \cdot 10^5$ | 180.04 | 1458.13 |
| $6.95 \cdot 10^5$ | 179.02 | 978.13 |
| $9.94 \cdot 10^5$ | 177.16 | 548.75 |
| $1.38 \cdot 10^6$, | 171.57 | 174.67 |
| $1.65 \cdot 10^6$ | 161.06 | 45.68 |
| $1.72 \cdot 10^6$ | 155.21 | 24.81 |
| $1.77 \cdot 10^6$ | 149.84 | 14.24 |
| $1.80 \cdot 10^6$ | 144.61 | 7.93 |
| $1.82 \cdot 10^6$ | 139.42 | 3.89 |

Table 5.1: Amplitudes, periods and stability indexes of the selected orbits for Sun-(Earth+Moon) system.

Table 5.2 shows the input simulation parameters: operational errors, mission constraints, control strategy and simulation time [11, 16].

| **Input Parameters** | |
|---|---|
| Number of orbits | 10 |
| OD errors | 1.5 km and 1 cm/s |
| OI errors | 150 km and 3 cm/s |
| Maneuver errors | 5% in magnitude |
| Tracking points | one per day |
| Min. time btw. maneuver | variable |
| Starting maneuver | 500 km |
| Limit maneuver | 50000 km |
| MC trials | 100 |
| $\mu$ | $3.04042 \cdot 10^{-6}$ [34] |

Table 5.2: Input parameters for Monte Carlo simulation in the Sun-(Earth+Moon) system

The *minimum time between maneuvers* is not fixed but variable, and will be chosen from time to time as a fraction of the orbital period. The notation used in plots to represent that parameter will be $\Delta t_{min}$.
Moreover, the results will be presented for one-axis and two-axes controllers. They have

been implemented as seen in Section 4.2.

Figure 5.3 shows the success probability of the station keeping algorithm implemented with the Floquet mode approach, as function of the $\Delta t_{min}$ and $A_z$. The first interesting observation that can be made is that the two-axis controller (Fig. 5.3b) provides an overall greater number of successes respect to one-axis controller (Fig. 5.3a), in particular higher amplitudes are better controlled. For both cases two common behaviours have been identified:

1. Increasing $\Delta t_{min}$ the station keeping starts to fail. However, for higher $A_z$ amplitudes, the station keeping algorithm starts to fail at higher $\Delta t_{min}$ than in the case of lower $A_z$.

2. Increasing the amplitudes $A_z$, even if $\Delta t_{min}$ is low, the station keeping fails.

The first behaviour is quite clear: increasing $\Delta t_{min}$ means that the station keeping is constrained to control less an orbit, thus, at a certain point it will fail. Since Halo orbits become more stable when $A_z$ increases, it is reasonable to think that, the station keeping that fails with a low amplitude orbit at a certain $\Delta t_{min}$, will succeed with the same $\Delta t_{min}$ but an higher amplitude orbit.
The reasons for the second behavior lie in the very structure of Floquet mode approach. Since the method aims to cancel the error state vector along the unstable component such that the s/c naturally converge on the nominal orbit, if the stable component is not so strong, the s/c will not able to converge on the nominal orbit. Remember, that the system is stable when the eigenvalues are within the unitary circle on the complex plane.

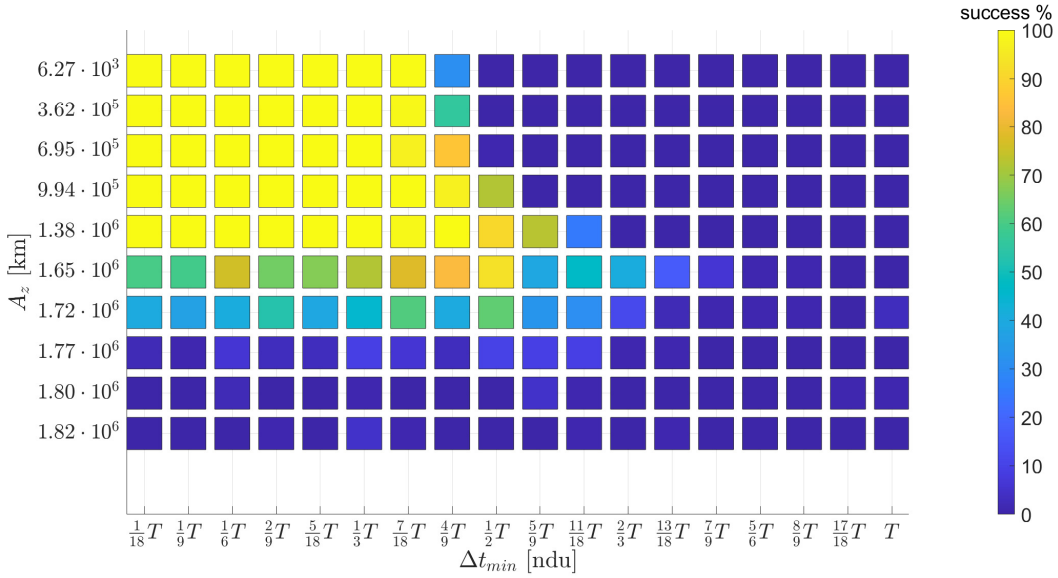


(a) One-axis controller

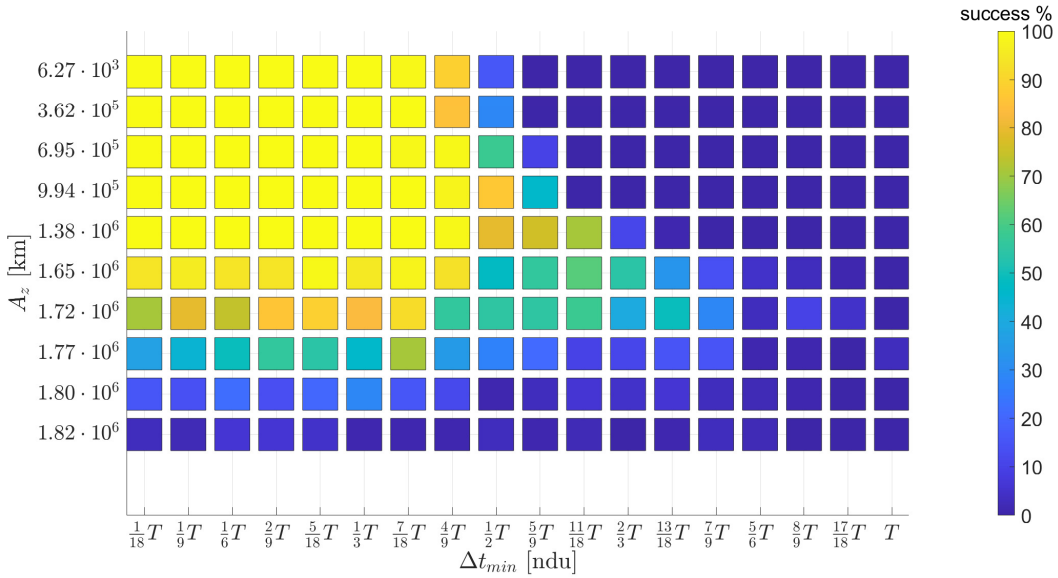


(b) Two-axis controller

Figure 5.3: Successes of Floquet mode approach: Halo orbits around $L_2$ in Sun-Earth system.

To better understand this behaviour, consider Fig. 5.4. Since the stable and unstable eigenvalues are the inverse of each other, low amplitude orbits, which are very unstable, have large value of the unstable component and thus a very small value of the stable component. On the other hand, higher amplitude orbits have small value of the unstable component but higher values of the stable component respect to low amplitude orbits. In addition, Fig. 5.4 highlights how at the beginning the unstable component decreases rapidly, while the stable component varies less. After that, the behaviour is the inverse

and the stable component change faster than the unstable one. For this reasons, in Fig. 5.4 is possible to identify two zones: success and failure zones. In the success zone the stable component is strong enough to keep a s/c bounded around a nominal orbit. In the failure zone, since the stable component increases, becoming less stronger, it will not able to keep the s/c bounded. Between the two zones, there is a transition region where the station keeping could succeed or not.

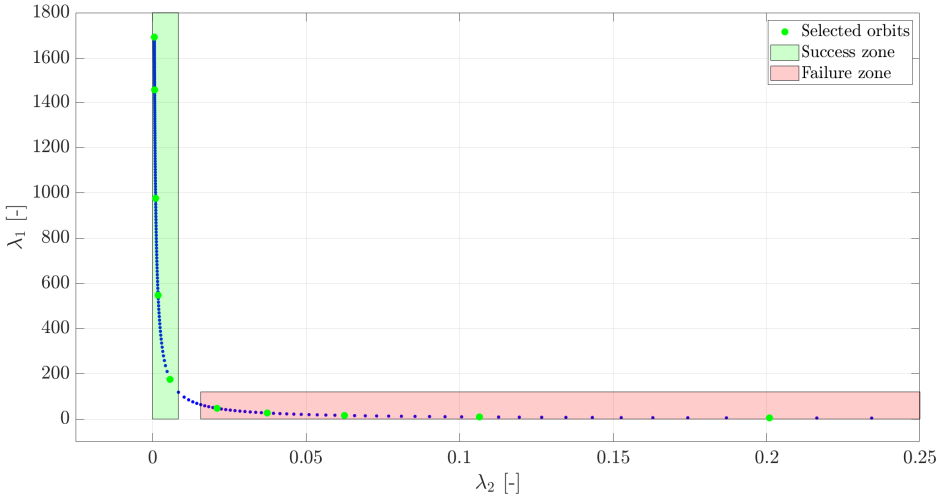


Figure 5.4: Unstable and stable eigenvalues of Halo orbits around L2 in Sun-(Earth+Moon) system.

These behaviours are more visible summing the successes for each orbit, as represented by Fig. 5.5. It is clear how at the beginning, in the success zone, the number of successes increasing since the orbits become more stable, but just as we enter in the failure zone, the success rate start to decrease. Moreover, it is visible how the two-axes controller, Fig. 5.5b, respect to the one axis-controller Fig. 5.5a, is more suitable for controlling larger amplitude orbits.

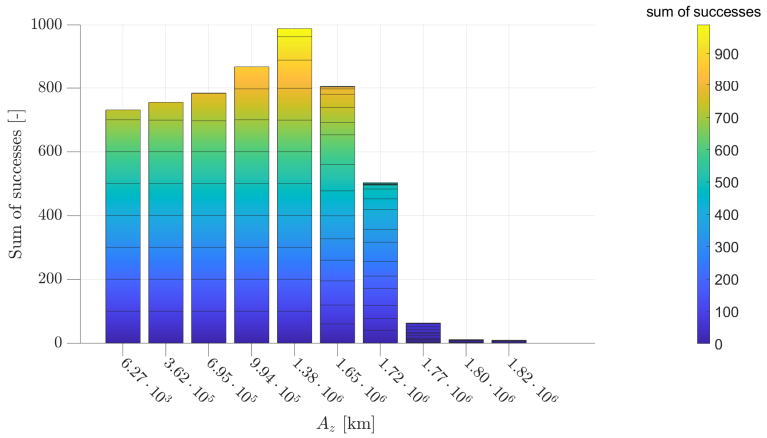


(a) One-axis controller

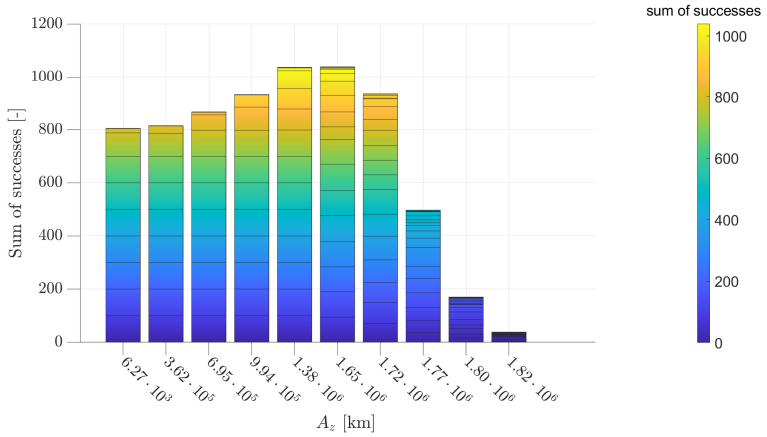


(b) Two-axis controller

Figure 5.5: Sum of successes of Floquet mode approach: Halo orbits around $L_2$ in Sun-(Earth+Moon) system.

### 5.2.2. Earth-Moon

In this Section the same kind of analysis is proposed for the Earth-Moon system. The selected orbits are shown in Fig. 5.6 and Table 5.3. Input parameters have been modified respect to the Sun-Earth case. Since Halo orbits in Earth-Moon system are much smaller than in the previous case, OI error in position, limit maneuver and starting maneuver have been changed, as described by Table 5.4.

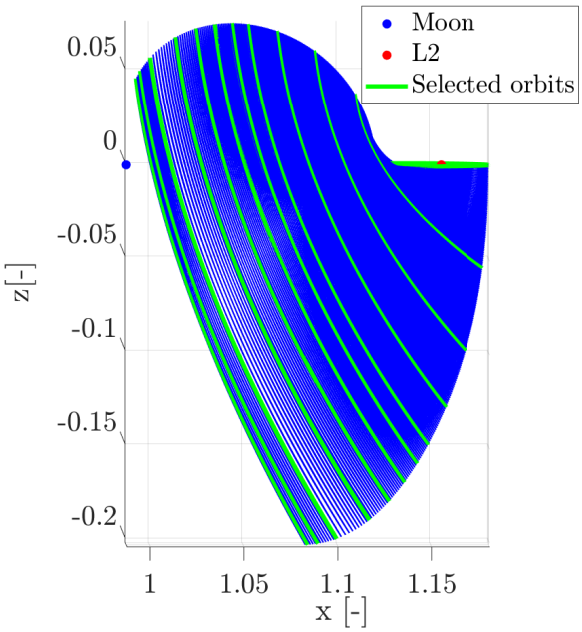


Figure 5.6: Earth-Moon systems selected orbits representation.

| $A_z$ [km] | T [days] | k |
|---|---|---|
| 38.44 | 14.83 | 1214.22 |
| $2.12 \cdot 10^4$ | 14.72 | 965.72 |
| $3.81 \cdot 10^4$ | 14.45 | 574.64 |
| $4.96 \cdot 10^4$ | 14.13 | 329.23 |
| $5.73 \cdot 10^4$ | 13.81 | 199.82 |
| $6.12 \cdot 10^4$ | 13.60 | 147.11 |
| $6.50 \cdot 10^4$ | 13.33 | 102.38 |
| $6.88 \cdot 10^4$ | 12.97 | 65.21 |
| $7.27 \cdot 10^4$ | 12.44 | 34.92 |
| $7.65 \cdot 10^4$ | 11.43 | 10 |
| $7.75 \cdot 10^4$ | 10.81 | 3.52 |
| $7.77 \cdot 10^4$ | 10.45 | 1.22 |

Table 5.3: Amplitudes, periods and stability indexes of the selected orbits for Earth-Moon system.

| **Input Parameters** | |
|---|---|
| Number of orbits | 10 |
| OD errors | 1.5 km and 1 cm/s |
| OI errors | 15 km and 3 cm/s |
| Maneuver errors | 5% in magnitude |
| Tracking points | one per day |
| Min. time btw. maneuver | variable |
| Starting maneuver | 100 km |
| Limit maneuver | 10000 km |
| MC trials | 100 |
| $\mu$ | 0.0121505 [34] |

Table 5.4: Input parameters for Monte Carlo simulation in the Earth-Moon system

The same conclusions drawn for the Sun-(Earth+Moon) system can be applied to the Earth-Moon system. Figure 5.7 shows the same two behaviours: the station keeping fails as $A_z$ and $\Delta t_{min}$ increase. However, more stable orbits can have grater $\Delta t_{min}$. Also in this case, the two-axes controller, Fig. 5.7b works better with respect to the one-axis controller Fig. 5.7a.

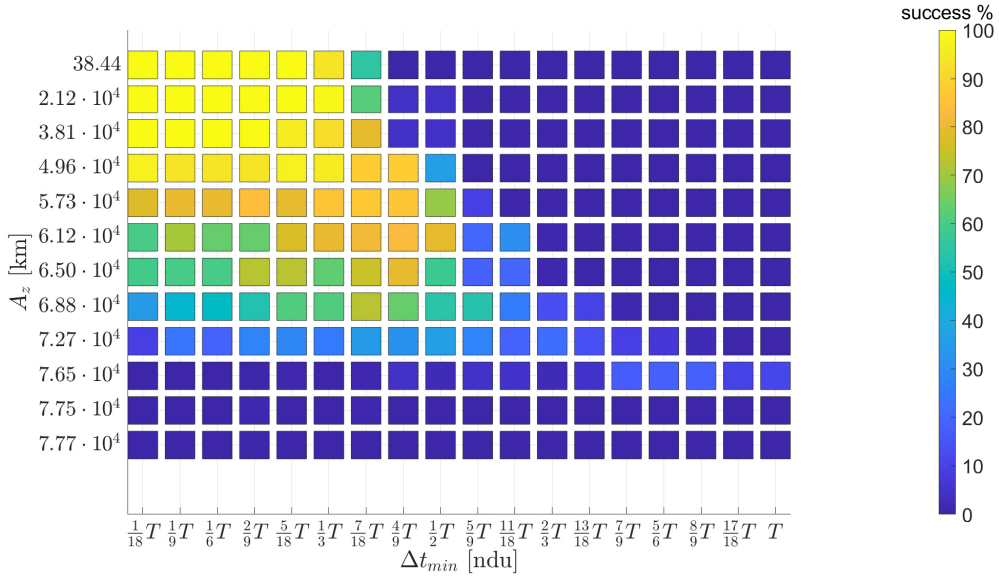


(a) One-axis controller

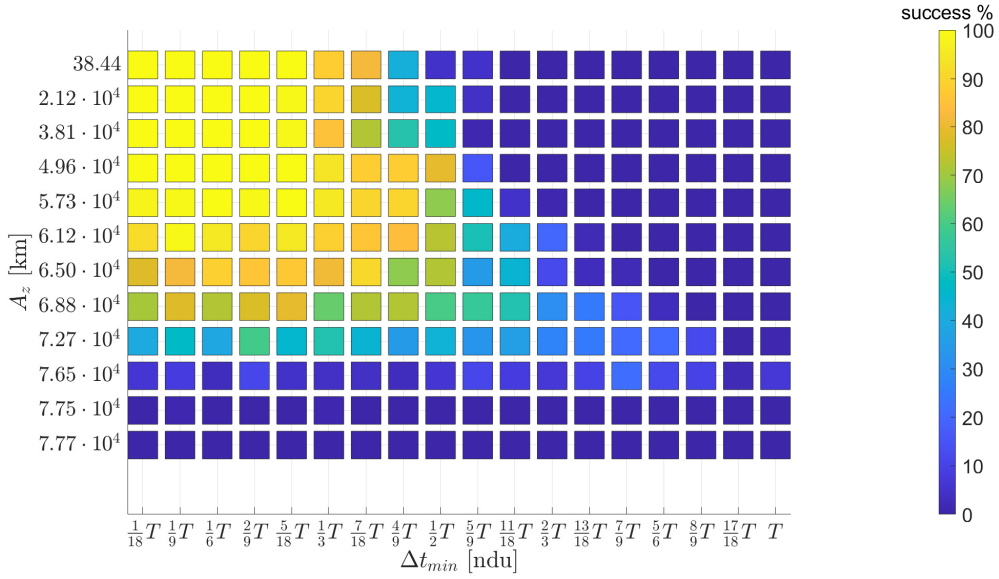


(b) Two-axis controller

Figure 5.7: Successes of Floquet mode approach: Halo orbits around $L_2$ in Earth-Moon system.

Figure 5.8 shows the failure and success zones. It is still evident how the station keeping has more successes for orbits with higher unstable component. Indeed, Fig. 5.9, as previously, shows that the success rate increases until the failure zone is reached.

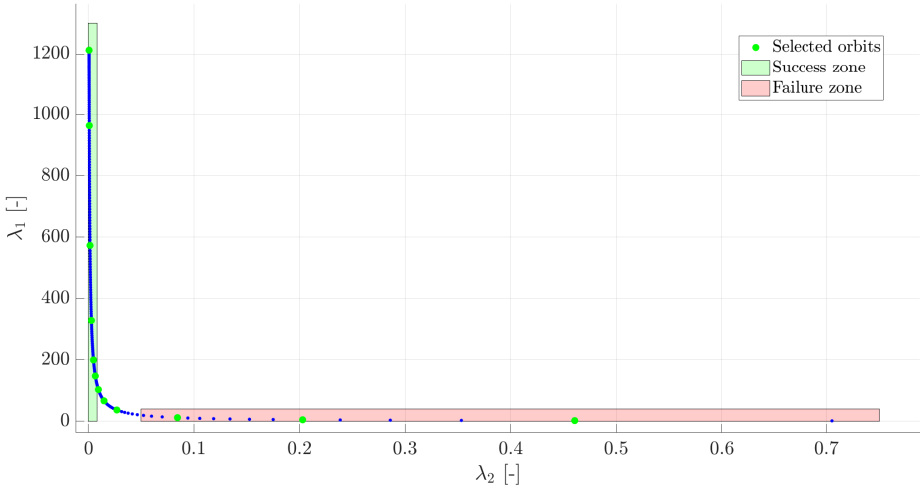


Figure 5.8: Unstable and stable eigenvalues of Halo orbits around L2 in Earth-Moon system.

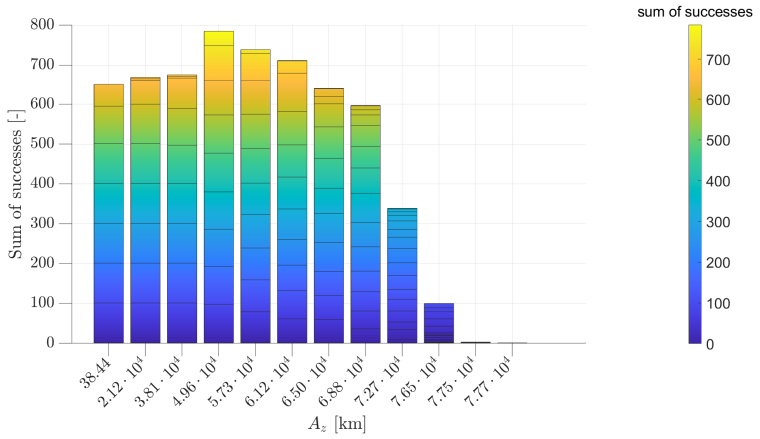


(a) One-axis controller

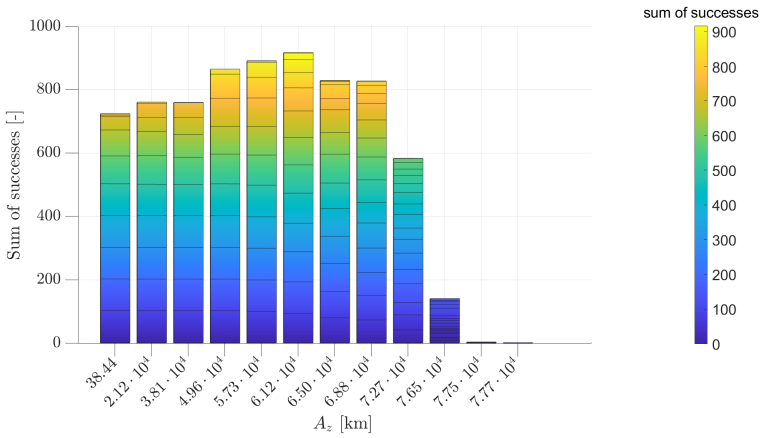


(b) Two-axis controller

Figure 5.9: Sum of successes of Floquet mode approach: Halo orbits around $L_2$ in Earth-Moon system.

## 5.3. Results

In this section, the main simulation results will be presented: station keeping cost, position error respect to the nominal orbit and the total number of necessary maneuvers. The cases considered are those where the station keeping has reached at least 90% of success. The parameter $\Delta t_{min}$ holds significance as it ensures greater flexibility for a mission. The choice of this parameter affects in different ways the presented results.

The number of maneuvers is strictly dependent from $\Delta t_{min}$, it is rapidly decreasing when $\Delta t_{min}$ increases, as represented by Figs. 5.10e, 5.11e, 5.12e and 5.13e. A propulsion system that has to work 30 times is more robust than one that has to work 100 times, thus the number of maneuvers is an important design parameter for a propulsion system.

The position error generally slightly increases when both $A_z$ and $\Delta t_{min}$ increase, as in Figs. 5.10c, 5.11c, 5.12c and 5.13c. The two-axes controller is, in general, more capable to keep a s/c bounded around a nominal orbit.

The cost of the station keeping instead increases when the $\Delta t_{min}$ increases, while since the orbits become more stable, when $A_z$ decreases, the cost slightly decreases, as in Figs. 5.10a, 5.11a, 5.12a and 5.13a. Again, the two-axis controller is able to keep station keeping costs lower with respect to the one-axis controller.

As mentioned above, the two-axes controller is able to control Halo orbits with higher amplitudes than the one-axis controller.

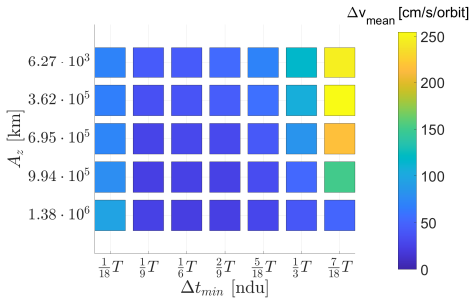


(a) Mean cost.

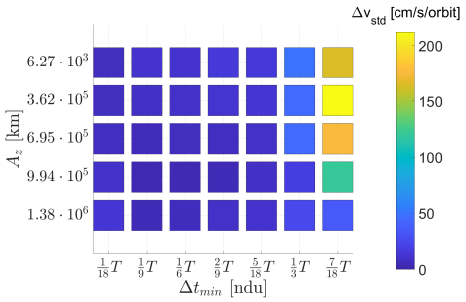


(b) STD cost.

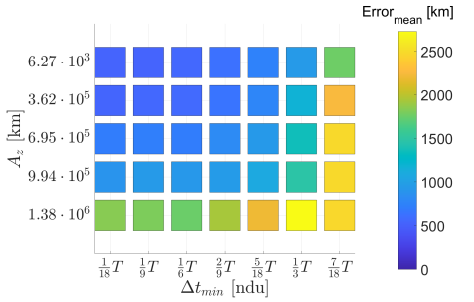


(c) Mean position error.

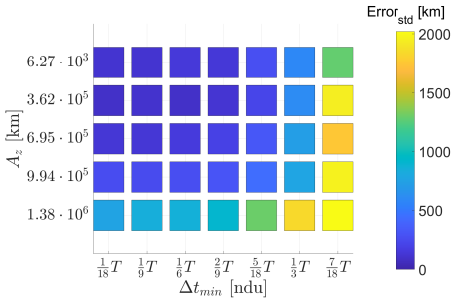


(d) STD position error.

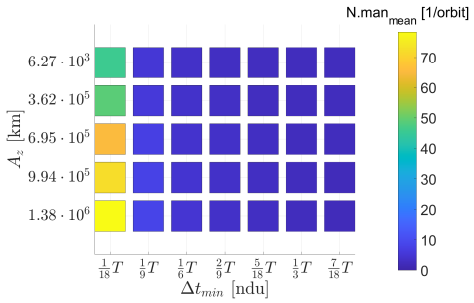


(e) Mean n° of maneuvers.

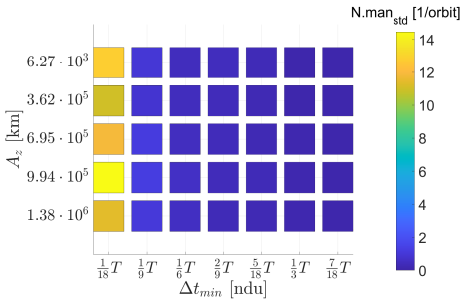


(f) STD n° of maneuvers.

Figure 5.10: Sun-(Earth+Moon) System: One-axis Controller.

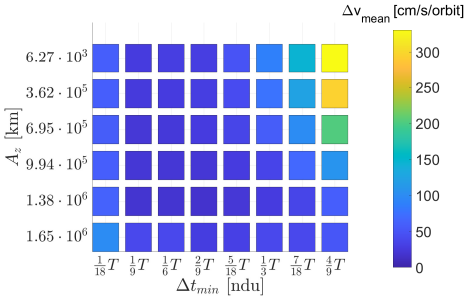


(a) Mean cost.

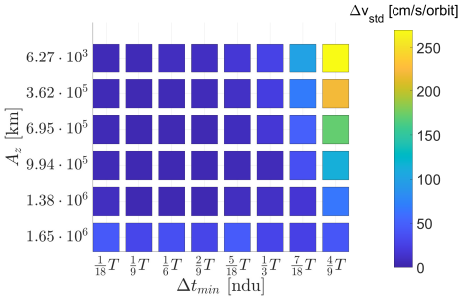


(b) STD cost.

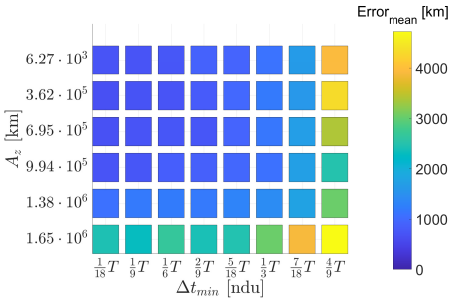


(c) Mean position error.

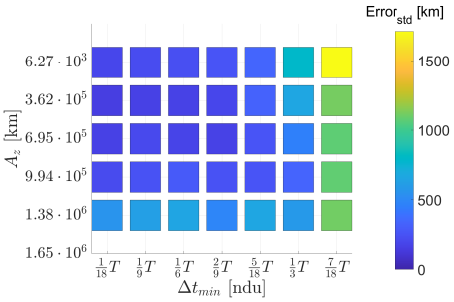


(d) STD position error.

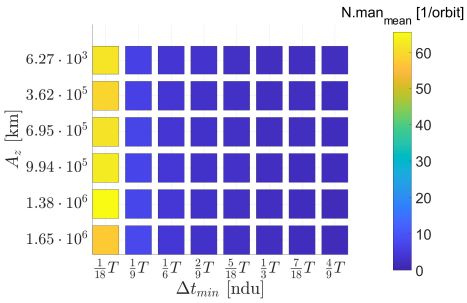


(e) Mean n° of maneuvers.

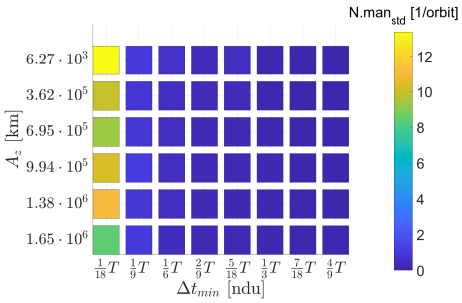


(f) STD n° of maneuvers.

Figure 5.11: Sun-(Earth+Moon) System: Two-axes Controller.

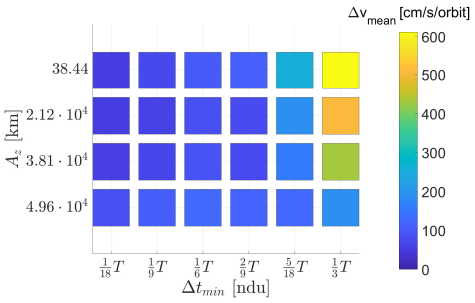


(a) Mean cost.

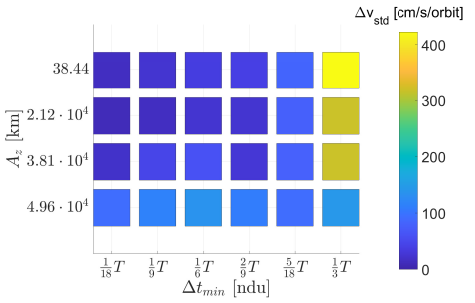


(b) STD cost.

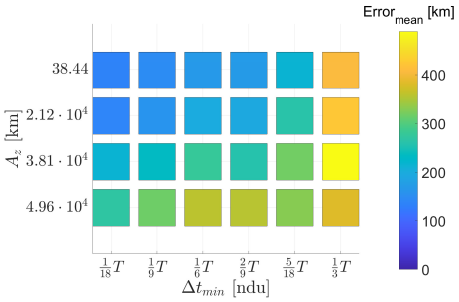


(c) Mean position error.

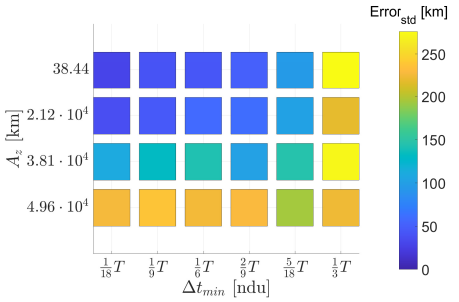


(d) STD position error.

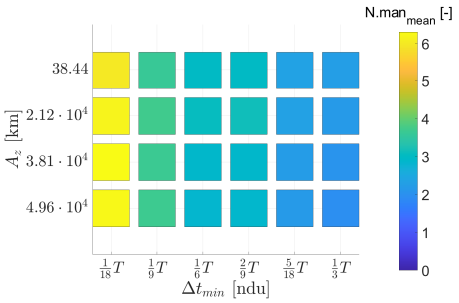


(e) Mean n° of maneuvers.

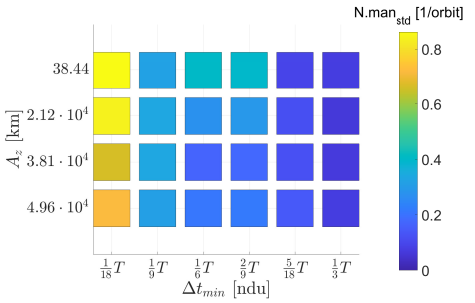


(f) STD n° of maneuvers.

Figure 5.12: Earth-Moon System: One-axis Controller.

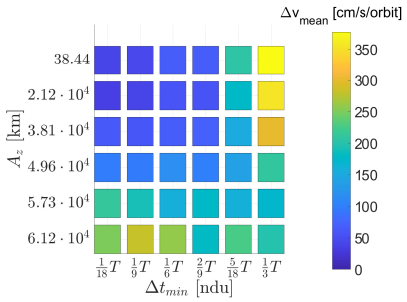


(a) Mean cost.

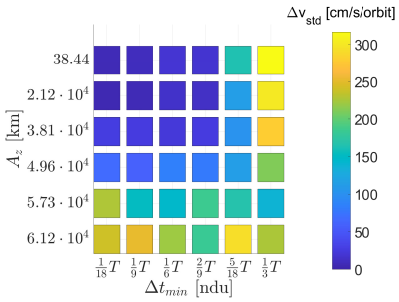


(b) STD cost.

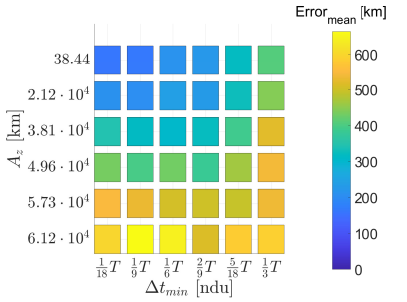


(c) Mean position error.

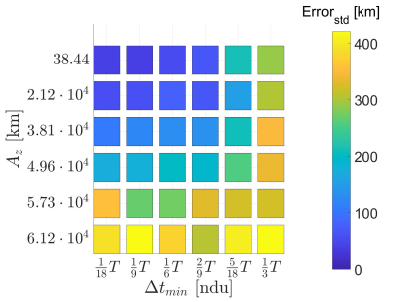


(d) STD position error.

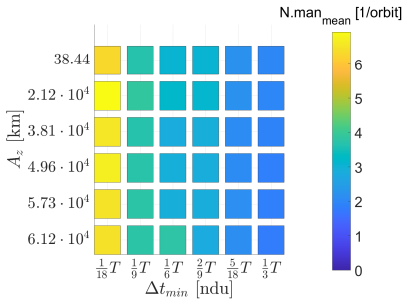


(e) Mean n° of maneuvers.

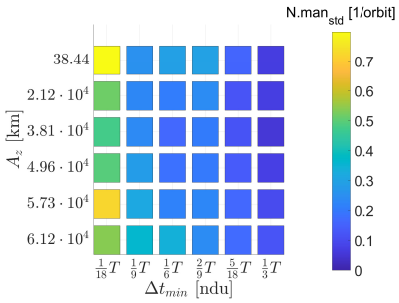


(f) STD n° of maneuvers.

Figure 5.13: Earth-Moon System: Two-axes Controller.

# 6 | Application

In this Section, two applications of the algorithm will be presented: one referring to the baseline operational orbit of the REMEC mission, the other will be an application in the BR4BP dynamics.

## 6.1. Application A: REMEC Mission

The REMEC mission [1] aims to monitor deep space from cosmic rays through the use of a CubeSat.It is a mission proposed by the European Space Agency (ESA). The mission analysis consisted in the development of a baseline [21] and backup [8] solution. Figure 6.1 shows the chosen orbits for the baseline option. The station keeping on the operational orbit and a preliminary analysis of the main perturbations affecting the s/c during the mission phases were performed on the baseline case's trajectories. All the data used in this thesis that describe physical and geometrical properties of the CubeSat derived from [1].

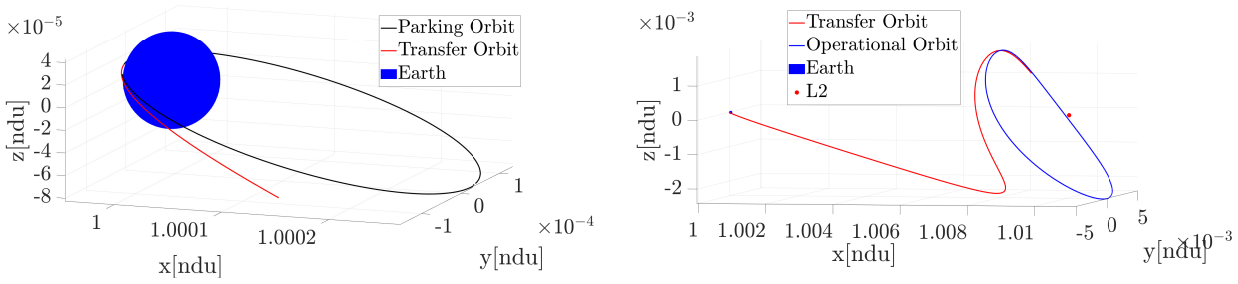


(a) Parking orbit representation (b) Transfer and operational orbits representation

Figure 6.1: REMEC mission's orbits.

### 6.1.1. Torque perturbations

Three kind of perturbations have been considered: Solar radiation pressure (SRP), Magnetic field, and Gravity gradient. Since this is a preliminary design the worst case conditions are considered. Here below the models[32, 36] are going to be presented:

**Solar Radiation Pressure**

Let's compute the SRP at 1AU:

$$P_{AU} = \frac{SF}{c} = 4.556 \cdot 10^{-6} \frac{N}{m^2} \tag{6.1}$$

Where the Solar flux $SF = 1367 W/m^2$ and the speed velocity $c = 3 \cdot 10^8 m/s$.

At this point, the value obtained in Eq. (6.1) needs to be scaled at the s/c distance:

$$P_{SC} = P_{AU} \left( \frac{1AU}{r_{sun-sc}} \right)^2 \left[ \frac{N}{m^2} \right] \tag{6.2}$$

Where $r_{sun-sc}$ is the distance between the Sun and the spacecraft. The maximum torque can be computed as:

$$T_{srp-max} = P_{SC} A_{SC} \rho_r (c_{ps} - c_g) \; [N \cdot m] \tag{6.3}$$

Where

- $A_{SC} = [1.570604; 2.728604] \; m^2$: for Chemical Propulsion (CP) and Electric Propulsion (EP) respectively; Surface area hits by the Sun.
- $\rho_r = [1.2; 1.8]$: reflectivity coefficients.
- $(c_{ps} - c_g) = 1.8 \; cm$: distance between the centres of pressure and gravity (worst case).

The SRP is going to be largest disturbance for the whole lifetime mission; thus it is modelled for all mission phases.

**Gravity Gradient**

The maximum torque due to the gravity gradient is computed as:

$$T_{gg-max} = \frac{3 G m_e}{2 r^3_{Earth-sc}} |I_M - I_m| \; [N \cdot m] \tag{6.4}$$

Where,

- $G$: Gravitational constant.
- $m_e$: Earth mass.

- $r_{Earth-sc}$: Earth-s/c distance.
- $|I_M - I_m|$: Difference between the maximum and minimum s/c inertia moments.

The moment of inertia used are different for the Beginning Of Life (BOL), End Of Life (EOL) and cruise phase:

- BOL: $\boldsymbol{I} = [4.40; 7.84; 10.42]\ kg\ m^2$
- EOL: $\boldsymbol{I} = [3.56; 3.71; 6.32] kg\ m^2$
- Cruise: $\boldsymbol{I} = [3.68; 4.32; 6.94] kg\ m^2$

### Magnetic torque

The dipole model is used to approximate the magnetic field and the torque due to magnetic field is computed with the following formula:

$$T_{mag-max} = B\ m_{mag}\ [N \cdot m] \tag{6.5}$$

Where,

- $m_{mag} = 0.1\ Am^2$: norm of parasitic magnetic induction (worst case).
- $B$: norm of magnetic field at spacecraft distance.

The magnetic field is approximated with a harmonic expansion model at first order, after the geosynchronous distance that model is no more valid since the solar wind modify the magnetic field. For this reason, the magnetic torque is modeled only for the parking orbit, moreover, it will be orders of magnitude less than SRP far from Earth.

Figure 6.2a shows how the torque due to SRP is higher than the Gravity Gradient (GG) and magnetic torques for the most orbital period. GG and magnetic torques become greater when the spacecraft passes near to the Earth. The SRP's torques are shown for different reflectivity coefficient and areas.
As visible in Fig. 6.2b, right after the s/c goes far from the Earth the SRP becomes the biggest torque disturbance and it has the same behavior as in the parking orbit, while GG decrease rapidly.
Fig. 6.2c shows that for the operational orbit the same conclusions of the transfer orbit can be done. The GG's torque is dependent by moment of inertia that are different for cruise and EOL phases, but the difference is so small that graphically the curves are overlapped.

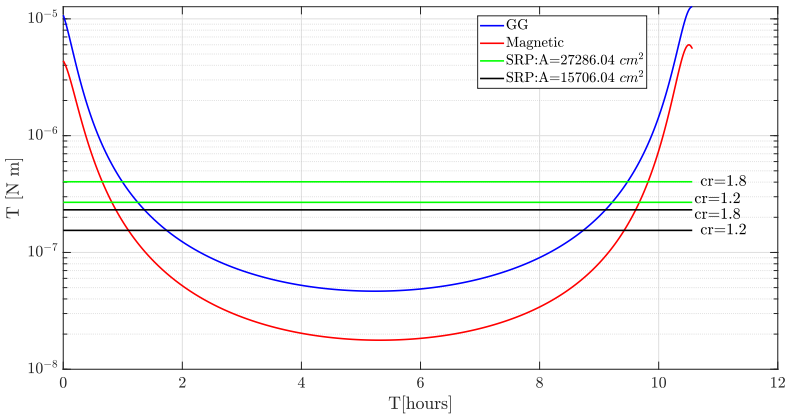


(a) Disturbance torques on the parking orbit at BOL.

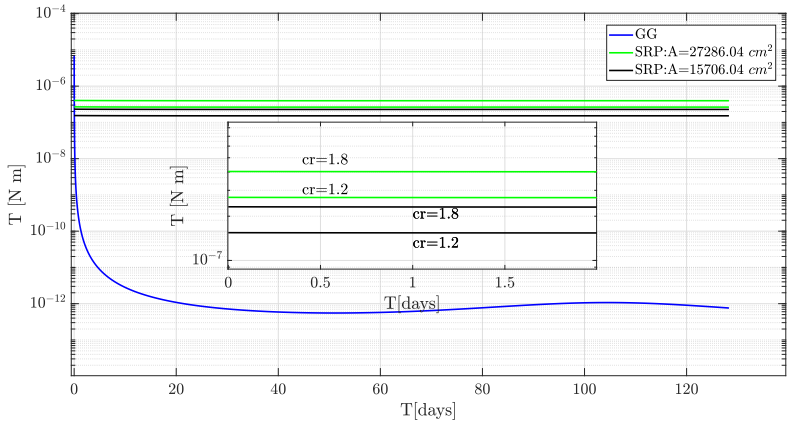


(b) Disturbance torques on the transfer orbit at cruise

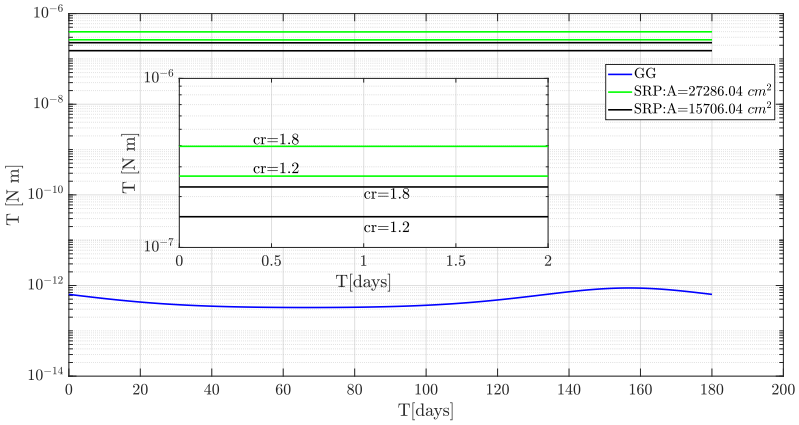


(c) Disturbance torques on the operational orbit at cruise and EOL

Figure 6.2: Perturbations on REMEC mission orbits.

### 6.1.2. Station keeping

The objective of station keeping for this application was to have a preliminary knowledge of the costs of orbit maintaining.
The operational orbit selected [21] has an amplitude $A_z = 280000\ km$ with the initial conditions shown in Table 6.1 and a period of about 180 days.

| x[ndu] | y[ndu] | z[ndu] | $\dot{x}$[ndu] | $\dot{y}$[ndu] | $\dot{z}$[ndu] |
|---|---|---|---|---|---|
| 1.008020 | 0 | 0.001871 | 0 | 0.011098 | 0 |

Table 6.1: Initial conditions of the REMEC mission operational orbit

The input simulation parameters have to be defined: operational errors, mission constraints, control strategy and simulation time. They are shown in Table 6.2.

| Input Parameters | |
|---|---|
| Number of orbits | 10 |
| OD errors | 1.5 km and 1 cm/s |
| OI errors | 150 km and 3 cm/s |
| Maneuver errors | 5% in magnitude |
| Tracking points | one per day |
| Min. time btw. maneuver | 30 days |
| Starting maneuver | 500 km |
| Limit maneuver | 50000 km |

Table 6.2: Input parameters for the station keeping algorithm for REMEC mission

Two results will be shown, one without and the other with the effect of solar radiation pressure affecting the s/c dynamics. The SRP was introduced into the dynamics using the cannonball model [32], so the s/c is assumed to be a spherical object with distributed optical properties, hits by the Sun. Equation (3.17) has been modified to introduce the effect of the SRP:

$$\begin{cases} x'' - 2y' = V_x + a_{sx}, \\ y'' + 2x' = V_y + a_{sy}, \\ z'' = V_z + a_{sz}. \end{cases} \tag{6.6}$$

Where $a_{sx}$,$a_{sx}$ and $a_{sx}$ are the acceleration components of the SRP. The SRP acceleration

can be computed as:

$$a_s = \frac{P_{SC} A_{SC}}{m_{SC}} \rho_r \tag{6.7}$$

Where the mass of the s/c is $m_{SC} = 100\ kg$, $A_{SC} = 1.570604\ m^2$ and $\rho_r = 1.8$.
At this point, the simulation can be performed by conducting 100 trials to obtain statistically significant results. Thus, following the procedure in Section 4.4 the main results obtained are reported in Table 6.3.

| | no SRP | | with SRP | |
|---|---|---|---|---|
| | **Mean** | **STD** | **Mean** | **STD** |
| **Error** | 612.15 km | 89.60 km | 8550.39 km | 1112.63 km |
| **SK cost** | 4.04 m/s | 1.01 m/s | 69.55 m/s | 5.11 m/s |
| **n° maneuver** | 33 | 3 | 44 | 1 |

Table 6.3: Simulation results REMEC mission.

To get an idea of what happens during the simulation, some graphic representations of a test simulation for both cases are provided. It is important to emphasise that in the case with SRP, eclipses are not present and that the affected surface is the same throughout the overall simulation time, thus it is a worst case scenario. The orbits are in both cases controlled, as shown in Figs. 6.3a and 6.3b, but the one with SRP seems to have a behavior such that the s/c drifts from the nominal orbit over time. The error in the case without SRP is bounded, Fig. 6.3c, while that with SRP diverges over time, Fig. 6.3d. Figures 6.3e and 6.3f show that the manoeuvre is performed when the unstable component is maximum, and then decreases immediately thereafter. Moreover, in the case with SRP the values are larger, increase in time and are all shifted in the same direction.
More plots about the evolution of errors can be found in Appendix B.1.

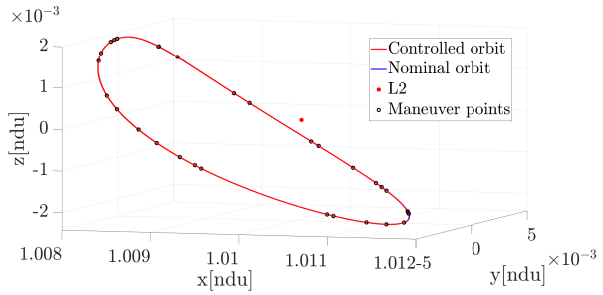


(a) Controlled orbit representation (no SRP).

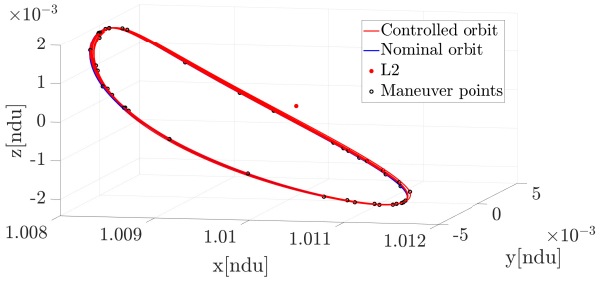


(b) Controlled orbit representation (with SRP).

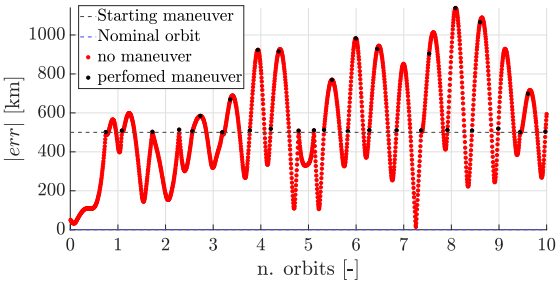


(c) Error norm (no SRP).

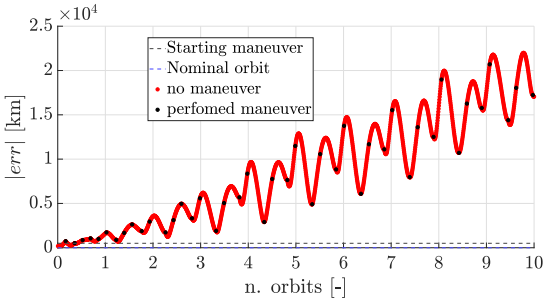


(d) Error norm (with SRP).

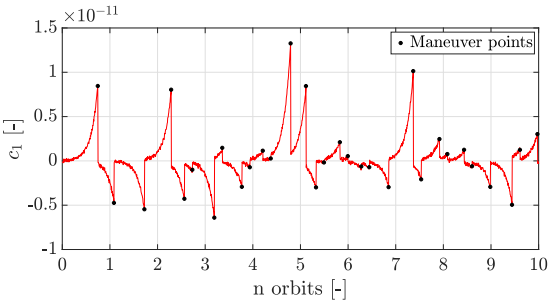


(e) Unstable component (no SRP).

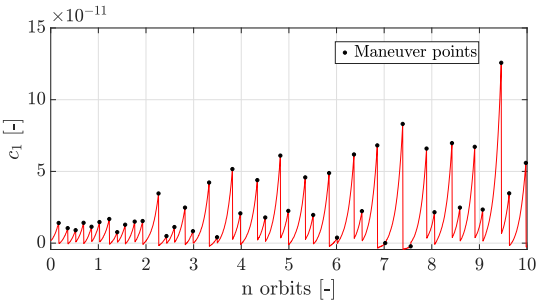


(f) Unstable component (with SRP).

Figure 6.3: Comparison between station keeping with and without SRP.

## 6.2. Application B: BR4BP

An application of the station keeping algorithm in the framework of BR4PP is shown. The dynamics in BR4BP has already been presented in Section 3.3.

Future developments of the REMEC mission operational orbit aim to refine what was previously identified as the baseline case in a more complete and realistic dynamical model, as in BR4BP. Since the initial conditions (Table 6.1) are found and integrated in the CR3BP environment, the same initial conditions and thus the orbit itself don't exist in this new dynamics. Figure 6.4 shows how the initial conditions integrated in the BR4BP dynamics does not give a closed orbit.

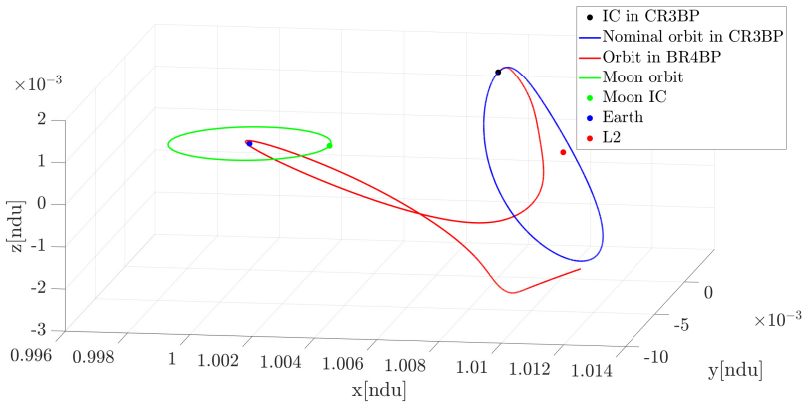


Figure 6.4: Orbit in BR4BP environment computed with initial conditions of the CR3BP .

There are two possible ways to solve this problem: either recompute the new initial conditions in the new dynamics or keep the same initial conditions used in CR3BP and use the station keeping algorithm to control the orbit in the BR4BP dynamics. The second option was selected.
Performing the station keeping with the same input values of Table 6.2, with the only difference in *Limit maneuver*= 500000 *km*, the results obtained with 100 trials are reported in Table 6.4.

| | **Mean** | **STD** |
|---|---|---|
| **Error** | 124934.33 km | 7472.16 km |
| **SK cost** | 2210.51 m/s | 266.89 m/s |
| **n° maneuver** | 49 | 1 |

Table 6.4: Simulation results in BR4BP.

The results are worse than in the CR3BP case, but were predictable as the Moon is introduced as a perturbation and therefore the station keeping algorithm has to compensate for it. However the SK is able to keep the orbit bounded as shown in Fig. 6.5.

For this reason, a reference orbit in the BR4BP can be calculated using the station keeping algorithm in order to be used as an initial guess for future refinement. To compute this reference orbit the input parameters have to be changed, as defined in Table 6.5. In this way the resulting controlled orbit is not affect by operational errors and mission constraints. The result of the simulation can be seen in Fig. 6.6. Important to note that the mean error in this case is equal to 12299.15 km.

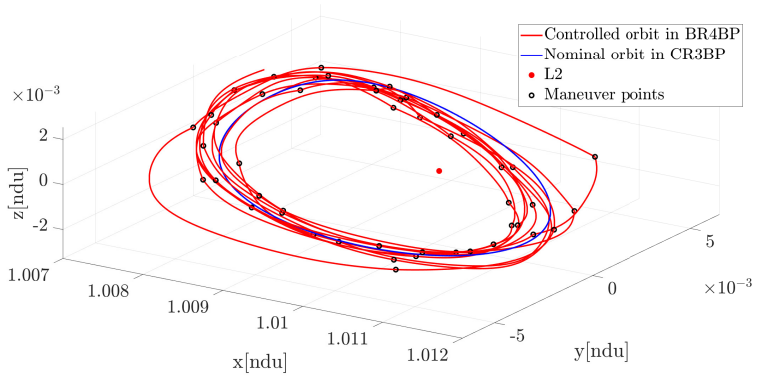


Figure 6.5: Controlled orbit in BR4BP computed with initial conditions of the CR3BP .

| Input Parameters | |
|---|---|
| Number of orbits | 1 |
| OD errors | 0 |
| OI errors | 0 |
| Maneuver errors | 0 |
| Tracking points | one per day |
| Min. time btw. maneuver | 1 days |
| Starting maneuver | 100 km |
| Limit maneuver | 500000 km |

Table 6.5: Input parameters to compute a reference orbit in BR4BP

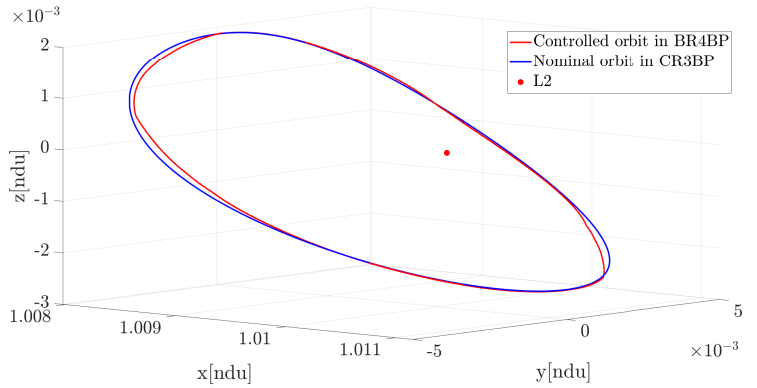


Figure 6.6: Controlled orbit in BR4BP to use as initial guess for future refinement.

# 7 | Conclusion

In this thesis, the Floquet mode approach method has been implemented and deeply studied, for Halo orbits in $L_2$ for Sun-(Earth+Moon) and Earth-Moon systems. As shown in Chapter 5, FMA has some limits of application. Since FMA exploits stable component to keep the s/c bounded around the nominal orbits, Halo orbits with a small unstable component, and therefore a larger stable component, are more difficult to control than orbits with a higher unstable component. In addition, the FMA was implemented by varying the minimum time between maneuvers $\Delta t_{min}$ and amplitude $A_z$ of the Halo orbits, to see how the algorithm was influenced by these parameters. As a general consideration, performances can be improved implementing a two-axes controller.
Within the identified operating limits, two applications were made. Application A: on the REMEC mission, where a preliminary evaluation of station keeping cost and about main perturbations were needed. The results were in agreement with literature (Table 2.1,[6, 11, 12, 30, 31]). In this application the station keeping was implemented also with SRP. Application B: station keeping was tested inside the BR4BP to verify if it was able to control a s/c. It turned out that the FMA was able to keep a s/c bounded around a nominal orbit, even if the station keeping costs are not reasonable.

## 7.1. Future works

As just said, FMA has some limitations, specifically respect to orbits with a very little unstable component. For this reason, it is suggested to perform the same analysis as described in Chapter 5, implementing another method, such as Hamiltonian Structure Preserving to check whether this method is able to control all orbits of the Halo family. Moreover, since an orbit in BR4BP has been computed using the FMA, this orbit can be used as initial guess for future refinement of the same orbit but in the four-body dynamics.

# A | Circular Restricted Three Body Problem

## A.1. Equation of motion in rotating frame

As described in [5], the position vector of the s/c is defined according to Fig. 3.3:

$$\boldsymbol{r}_d = x_d\hat{\boldsymbol{i}} + y_d\hat{\boldsymbol{j}} + z_d\hat{\boldsymbol{k}} \tag{A.1}$$

Then Eq. (A.1) has to be derived twice:

$$\boldsymbol{v}_d = \frac{d\boldsymbol{r}_d}{dt} = \dot{x}_d\hat{\boldsymbol{i}} + x_d\frac{d\hat{\boldsymbol{i}}}{dt} + \dot{y}_d\hat{\boldsymbol{j}} + y_d\frac{d\hat{\boldsymbol{j}}}{dt} + \dot{z}_d\hat{\boldsymbol{k}} + z_d\cancelto{0}{\frac{d\hat{\boldsymbol{k}}}{dt}} = \frac{\partial\boldsymbol{r}_d}{\partial t} + (\boldsymbol{\omega}\times\boldsymbol{r}_d) \tag{A.2}$$

$$\boldsymbol{a}_d = \frac{d\boldsymbol{v}_d}{dt} = \frac{\partial\boldsymbol{v}_d}{\partial t} + (\boldsymbol{\omega}\times\boldsymbol{v}_d) = \frac{\partial}{\partial t}\left(\frac{\partial\boldsymbol{r}_d}{\partial t} + (\boldsymbol{\omega}\times\boldsymbol{r}_d)\right) + \boldsymbol{\omega}\times\left(\frac{\partial\boldsymbol{r}_d}{\partial t} + (\boldsymbol{\omega}\times\boldsymbol{r}_d)\right)$$

$$= \frac{\partial^2\boldsymbol{r}_d}{\partial t^2} + \cancelto{0}{\dot{\boldsymbol{\omega}}}\times\boldsymbol{r}_d + \boldsymbol{\omega}\times\frac{\partial\boldsymbol{r}_d}{\partial t} + \boldsymbol{\omega}\times\frac{\partial\boldsymbol{r}_d}{\partial t} + \boldsymbol{\omega}\times(\boldsymbol{\omega}\times\boldsymbol{r}_d) \tag{A.3}$$

$$= \frac{\partial^2\boldsymbol{r}_d}{\partial t^2} + \boldsymbol{\omega}\times(\boldsymbol{\omega}\times\boldsymbol{r}_d) + 2\boldsymbol{\omega}\times\frac{\partial\boldsymbol{r}_d}{\partial t}$$

Since the $z$ axis of rotating frame coincides with $\hat{Z}$ axis of inertial frame and the assumption of circular motion has been already introduced: $d\boldsymbol{k}/dt = 0$ and $\dot{\boldsymbol{\omega}} = 0$. Using second Newton's law, Newton's law of universal gravitation and Eq. (A.3) can be written as:

$$\ddot{\boldsymbol{r}}_d + 2\boldsymbol{\omega}\times\dot{\boldsymbol{r}}_d + \boldsymbol{\omega}\times(\boldsymbol{\omega}\times\boldsymbol{r}_d) = \frac{1}{m}(\boldsymbol{F}_{\mathbf{1}d} + \boldsymbol{F}_{\mathbf{2}d}) = -G\frac{m_1}{r_{1d}^3}\boldsymbol{r}_{\mathbf{1}d} - G\frac{m_2}{r_{2d}^3}\boldsymbol{r}_{\mathbf{2}d} \tag{A.4}$$

Since $\boldsymbol{\omega} = \left[0, 0, n\hat{\boldsymbol{k}}\right]^T$, the vectorial products are:

- $2\boldsymbol{\omega} \times \dot{\boldsymbol{r}}_d = -2\omega\dot{y}_d\hat{\boldsymbol{i}} + 2\omega\dot{x}_d\hat{\boldsymbol{j}}$
- $\boldsymbol{\omega} \times (\boldsymbol{\omega} \times \boldsymbol{r}_d) = -\omega^2 x_d\hat{\boldsymbol{i}} - \omega^2 y_d\hat{\boldsymbol{j}}$

At this point, substituting also $m_1 = (1-\mu)M$, $m_2 = \mu M$, $d_1 = \mu l$ and $d_2 = (1-\mu)l$, Eq. (A.4) can be written as:

$$\begin{cases} \ddot{x}_d - 2n\dot{y}_d - n^2 x_d = -GM\left[\dfrac{1-\mu}{r_{1d}^3}(x_d + \mu l) + \dfrac{\mu}{r_{2d}^3}(x_d - (1-1\mu)l)\right], \\ \ddot{y}_d + 2n\dot{y} - n^2 y = -GM\left[\dfrac{1-\mu}{r_{1d}^3}y_d + \dfrac{\mu}{r_{2d}^3}y_d\right], \\ \ddot{z}_d = -GM\left[\dfrac{1-\mu}{r_{1d}^3}z_d + \dfrac{\mu}{r_{2d}^3}z_d\right]. \end{cases} \tag{A.5}$$

## A.2. Dimensionless equation of motion in rotating frame

Considering Eq. (3.14), let's first compute its time derivatives:

$$\begin{cases} x \quad \text{component:} \quad \dot{x} = nx' \quad \dot{x} = n^2 x'' \\ y \quad \text{component:} \quad \dot{y} = ny' \quad \dot{y} = n^2 y'' \\ z \quad \text{component:} \quad \dot{z} = nz' \quad \dot{x} = n^2 z'' \end{cases} \tag{A.6}$$

Now, substitute Eq. (A.6) into Eq. (A.5):

$$\begin{cases} n^2 x_d'' - 2n^2 y_d' - n^2 x_d = -GM\left[\dfrac{1-\mu}{r_{1d}^3}(x_d + \mu l) + \dfrac{\mu}{r_{2d}^3}(x_d - (1-1\mu)l)\right], \\ n^2 y_d'' + 2n^2 y' - n^2 y = -GM\left[\dfrac{1-\mu}{r_{1d}^3}y_d + \dfrac{\mu}{r_{2d}^3}y_d\right], \\ n^2 z_d'' = -GM\left[\dfrac{1-\mu}{r_{1d}^3}z_d + \dfrac{\mu}{r_{2d}^3}z_d\right]. \end{cases} \tag{A.7}$$

Since $GM/n^2 = l^3$ and $l^3/{r_d}^3 = 1/r^3$, divide Eq. (A.7) by $n^2$:

$$\begin{cases} x_d'' - 2y_d' - x_d = -\left[\dfrac{1-\mu}{r_1^3}(x_d + \mu l) + \dfrac{\mu}{r_2^3}(x_d - (1-1\mu)l)\right], \\ y_d'' + 2y_d' - y_d = -\left[\dfrac{1-\mu}{r_1^3}y_d + \dfrac{\mu}{r_2^3}y_d\right], \\ z_d'' = -\left[\dfrac{1-\mu}{r_1^3}z_d + \dfrac{\mu}{r_2^3}z_d\right]. \end{cases} \tag{A.8}$$

Having only components function of space, divide Eq. (A.8) by $l$ to obtain the final equations:

$$\begin{cases} x'' - 2y' - x = -\dfrac{1-\mu}{r_1^3}(x+\mu) - \dfrac{x+\mu-1}{r_2^3}\mu, \\ y'' + 2x' - y = -\dfrac{1-\mu}{r_1^3}y - \dfrac{\mu}{r_2^3}y, \\ z'' = -\dfrac{1-\mu}{r_1^3}z - \dfrac{\mu}{r_2^3}z. \end{cases} \tag{A.9}$$

## A.3. Jacobian matrix of the total potential

The dimensionless second partial derivatives [32] of the Jacobian are here reported for completeness.

$$\begin{cases} V_{xx} = 1 - \dfrac{1-\mu}{r_1^3}\left[1 - \dfrac{3(x-\mu)^2}{r_1^2}\right] - \dfrac{\mu}{r_2^3}\left[1 - \dfrac{3(x-(1-\mu))^2}{r_2^2}\right], \\ V_{yy} = 1 - \dfrac{1-\mu}{r_1^3}\left[1 - \dfrac{3y^2}{r_1^2}\right] - \dfrac{\mu}{r_2^3}\left[1 - \dfrac{3y^2}{r_2^2}\right], \\ V_{zz} = -\dfrac{1-\mu}{r_1^3}\left[1 - \dfrac{3z^2}{r_1^2}\right] - \dfrac{\mu}{r_2^3}\left[1 - \dfrac{3z^2}{r_2^2}\right], \\ V_{xy} = (1-\mu)\dfrac{3(x-\mu)y}{r_1^5} + \mu\dfrac{3(x-(1-\mu))y}{r_2^5}, \\ V_{xz} = (1-\mu)\dfrac{3(x-\mu)z}{r_1^5} + \mu\dfrac{3(x-(1-\mu))z}{r_2^5}, \\ V_{yz} = (1-\mu)\dfrac{3yz}{r_1^5} + \mu\dfrac{3yz}{r_2^5} \end{cases} \tag{A.10}$$

## A.4. State transition matrix

In case of small deviations from initial conditions the flow can be linearised:

$$\boldsymbol{\varphi}(\boldsymbol{x}_0 + \delta\boldsymbol{x}_0, t_0, t) = \boldsymbol{\varphi}(\boldsymbol{x}_0, t_0, t) + \frac{\partial\boldsymbol{\varphi}}{\partial\boldsymbol{x}_0}(\boldsymbol{x}_0, t_0, t)\delta\boldsymbol{x}_0 \tag{A.11}$$

Let's now substitute Eq. (A.11) into Eq. (3.30),

$$\boldsymbol{x} + \delta\boldsymbol{x} = \boldsymbol{\varphi}(\boldsymbol{x}_0, t_0, t) + \frac{\partial \boldsymbol{\varphi}}{\partial \boldsymbol{x}_0}(\boldsymbol{x}_0, t_0, t)\delta\boldsymbol{x}_0 \tag{A.12}$$

Since $\boldsymbol{x} = \boldsymbol{\varphi}(\boldsymbol{x}_0, t_0, t)$, Eq. (A.12) becomes:

$$\delta\boldsymbol{x} = \frac{\partial \boldsymbol{\varphi}}{\partial \boldsymbol{x}_0}(\boldsymbol{x}_0, t_0, t)\delta\boldsymbol{x}_0 \tag{A.13}$$

The Jacobian of the flow in Eq. (A.13) is a matrix and each component can be expressed as:

$$\frac{\partial \boldsymbol{\varphi}}{\partial \boldsymbol{x}_0}(\boldsymbol{x}_0, t_0, t) = \begin{bmatrix} \frac{\partial \varphi_x}{\partial x_0} & \frac{\partial \varphi_x}{\partial y_0} & \frac{\partial \varphi_x}{\partial z_0} & \frac{\partial \varphi_x}{\partial \dot{x}_0} & \frac{\partial \varphi_x}{\partial \dot{y}_0} & \frac{\partial \varphi_x}{\partial \dot{z}_0} \\ \frac{\partial \varphi_y}{\partial x_0} & \frac{\partial \varphi_y}{\partial y_0} & \frac{\partial \varphi_y}{\partial z_0} & \frac{\partial \varphi_y}{\partial \dot{x}_0} & \frac{\partial \varphi_y}{\partial \dot{y}_0} & \frac{\partial \varphi_y}{\partial \dot{z}_0} \\ \frac{\partial \varphi_z}{\partial x_0} & \frac{\partial \varphi_z}{\partial y_0} & \frac{\partial \varphi_z}{\partial z_0} & \frac{\partial \varphi_z}{\partial \dot{x}_0} & \frac{\partial \varphi_z}{\partial \dot{y}_0} & \frac{\partial \varphi_z}{\partial \dot{z}_0} \\ \frac{\partial \varphi_{\dot{x}}}{\partial x_0} & \frac{\partial \varphi_{\dot{x}}}{\partial y_0} & \frac{\partial \varphi_{\dot{x}}}{\partial z_0} & \frac{\partial \varphi_{\dot{x}}}{\partial \dot{x}_0} & \frac{\partial \varphi_{\dot{x}}}{\partial \dot{y}_0} & \frac{\partial \varphi_{\dot{x}}}{\partial \dot{z}_0} \\ \frac{\partial \varphi_{\dot{y}}}{\partial x_0} & \frac{\partial \varphi_{\dot{y}}}{\partial y_0} & \frac{\partial \varphi_{\dot{y}}}{\partial z_0} & \frac{\partial \varphi_{\dot{y}}}{\partial \dot{x}_0} & \frac{\partial \varphi_{\dot{y}}}{\partial \dot{y}_0} & \frac{\partial \varphi_{\dot{y}}}{\partial \dot{z}_0} \\ \frac{\partial \varphi_{\dot{z}}}{\partial x_0} & \frac{\partial \varphi_{\dot{z}}}{\partial y_0} & \frac{\partial \varphi_{\dot{z}}}{\partial z_0} & \frac{\partial \varphi_{\dot{z}}}{\partial \dot{x}_0} & \frac{\partial \varphi_{\dot{z}}}{\partial \dot{y}_0} & \frac{\partial \varphi_{\dot{z}}}{\partial \dot{z}_0} \end{bmatrix} \tag{A.14}$$

# B | REMEC application

## B.1. Evolution of component errors

Here below are presented a comparison between the evolution of component errors with and without SRP. In the case with SRP is evident how the errors are not bounded and increase in time. Moreover, Fig. B.1b shows how the error along x is shifted to the positive plane, a behaviour due to the SRP moving the s/c away.

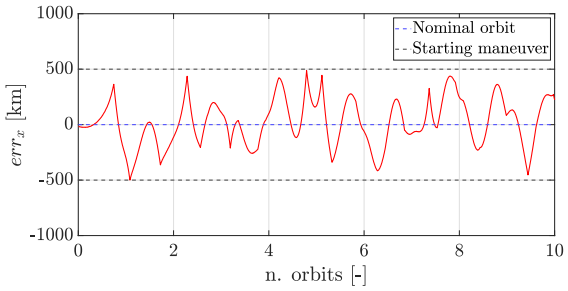


(a) Error component along x (no SRP).

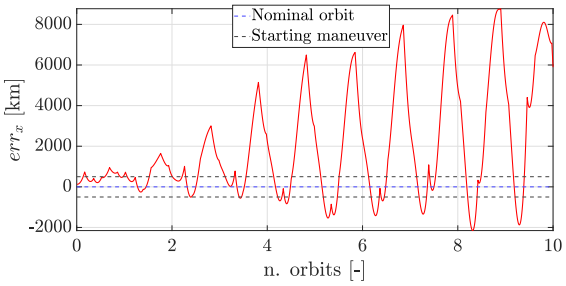


(b) Error component along x (with SRP).

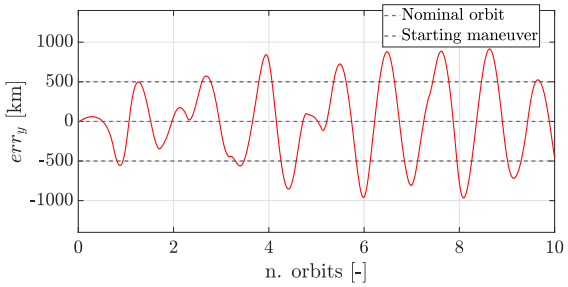


(c) Error component along y (no SRP).

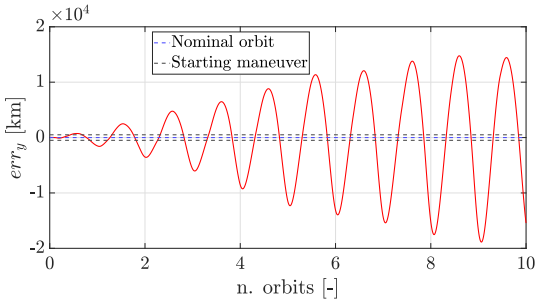


(d) Error component along y (with SRP).

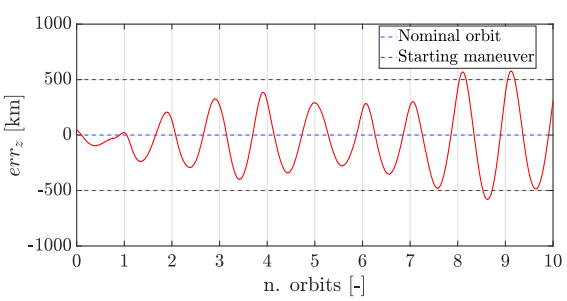


(e) Error component along z (no SRP).

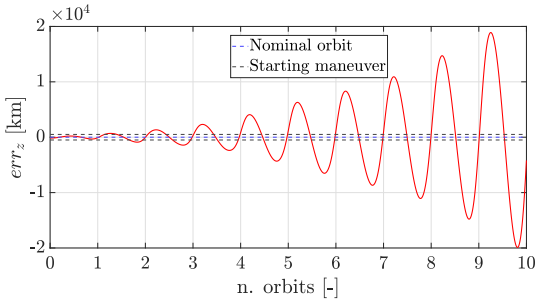


(f) Error component along z (with SRP).

Figure B.0: Comparison between evolution of component errors with and without SRP.

# Bibliography

[1] A. Aguilar, R. Filgas, C. Colombo, E. M. Alessi, M. lo Iacono, E. Arikan, and M. Bolis. The remec mission: Mission concept and architecture feasibility assessment. Technical report, 2023.

[2] J. V. Breakwell. Investigation of halo satellite orbit control. Technical report, Nasa, 1973.

[3] R. A. Broucke. Periodics orbits in the restricted three body problem with earth-moon masses. Technical report, JPL.

[4] E. Canalias, G. Gomez, M. Marcote, and J. Masdemont. Assessment of mission design including utilization of libration points and weak stability boundaries. Technical report, ESA Advanced Concept Team, 2004.

[5] G. Colasurdo and G. Avanzini. Astrodynamics. *Ch*, 6:88–90, 2006.

[6] S. Cravedi. Floquet modes approach. Master's thesis, Politecnico di Milano, 2019. Supervisor: Prof. Francesco Topputo.

[7] D. J. Dichmann, C. M. Alberding, and W. H. Yu. Stationkeeping monte carlo simulation for the james webb space telescope. Technical report, 2014.

[8] A. Enis. Transfer trajectory and operational orbit selection for earth-moon l2 near rectilinear halo orbits through invariant manifolds. Master's thesis, Politecnico di Milano, 2023. Supervisor: Prof. Camilla Colombo.

[9] R. W. Farquhar. The control and use of libration-point satellites. Technical report, Nasa, 1970.

[10] R. W. Farquhar and A. A. Kamel. Quasi-periodic orbits about the translunar libration point. *Celestial Mechanics and Dynamical Astronomy*, 1973. doi: 10.1007/BF01227511.

[11] A. Farrès, G. Gòmez, J. Masdemont, C. Webster, and D. C. Folta. In *The Geome-*

*try of Station-Keeping Strategies around Libration Point Orbits*. 70th International Astronautical Congress, IAF, 2019.

[12] G. Gomez, J. Llibre, R. Martinez, and C. Simò. *Dynamics and Mission Design Near Libration points*. World Scientific Publishing Co. Pte. Ltd., 2001. doi: 10.1142/4337.

[13] S. C. Gordon. *Orbit determination erro and analysis and station-keeping for libration point trajectories*. PhD thesis, Purdue University, West Lafayette, Indiana, 1991.

[14] D. J. Grebow. Generating periodic orbits in the circular restricted three-body problem with applications to lunar south pole coverage. Master's thesis, Purdue University, West Lafayette, Indiana, 2006.

[15] P. Gurfil and D. Meltzer. Stationkeeping on unstable orbits: Generalization to the elliptic restricted three-body problem. *Astronautical Sciences*, pages 29–51, 2006. doi: https://doi.org/10.1007/BF03256475.

[16] G. Gòmez, K. Howell, J. Masdemont, and C. Simò. Station-keeping strategies for translunar libration ppoint orbits. *Advances in the Astronautical Sciences*, 1998.

[17] K. C. Howell and H. Pernicka. Stationkeeping method for libration point trajectories. *Journal of Guidance, Control, and Dynamics*, 1993. doi: https://doi.org/10.2514/3.11440.

[18] A. Jorba and J. Masdemont. Dynamics in the centre manifold of the collinear points of the restricted three body problem. *Physica D Nonlinear Phenomena*, 1998. doi: http://dx.doi.org/10.1016/S0167-2789(99)00042-1.

[19] T. M. Keeter. Station-keeping strategies for libration point orbits: Target point and floquet mode approaches. Master's thesis, Purdue University, West Lafayette, Indiana, 1994.

[20] W. S. Koon, M. W. Lo, J. E. Marsden, and S. D. Ross. *Dynamical Systems, the Three-Body Problem and Space Mission Design*. Marsden Books., 2006. ISBN 978-0-615-24095-4.

[21] M. Lo Iacono. Parametric design for earth to sun-earth l2 halo transfers in the circular restricted three body problem. Master's thesis, Politecnico di Milano, 2023. Supervisor: Prof. Camilla Colombo.

[22] G. Mingotti and F. Topputo. Ways to the moon: a survey. *Advances in the Astronautical Sciences*, 2011.

[23] NASA/WMAP Science Team. Lagrange points, 2018. URL `https://solarsystem.nasa.gov/resources/754/what-is-a-lagrange-point/`.

[24] T. A. Pavlak. *Trajectory Desing and Orbit Maintenance Strategies in Multy-Body Dynamical Regimes*. PhD thesis, Purdue University, West Lafayette, Indiana, 2013.

[25] J. Petersen. L2 station keeping maneuver strategy for the james webb space telescope. Technical report, 2019.

[26] R. Qi and S. Xu. Optimal low-thrust transfers to lunar l1 halo orbit using variable specific impulse engine. *Journal of Aerospace Engineering*, 2014. doi: https://doi.org/10.1061/(ASCE)AS.1943-5525.0000432.

[27] D. L. Richardson. Analytical construction of periodic orbits about the collinear points. *Celestial Mechanics*, 1979. doi: https://doi.org/10.1007/BF01229511.

[28] D. J. Scheeres, F. Y. Hsiao, and V. N. X. Stabilizing motion relative to an unstable orbit: Applications to spacecraft formation flight. *Journal of Guidance, Control, ans Dynamics*, 2003. doi: 10.2514/2.5015.

[29] K. Shahid and K. D. Kumar. Stationkeeping method for libration point trajectories. *Journal of Spacecraft and rockets*, 2010. doi: http://dx.doi.org/10.2514/1.47342.

[30] M. Shirobokov, S. Trofimov, and M. Ovchinnikov. Survey of station-keeping techniques for libration point orbits. *Journal of Guidance, Control, ans Dynamics*, 2017. doi: https://doi.org/10.2514/1.G001850.

[31] C. Simò, G. Gomez, J. Llibre, R. Martinez, and J. Rodriguez. On the optimal station keeping control of halo orbits. *Acta Astronautica*, pages 391–397, 1987. doi: https://doi.org/10.1016/0094-5765(87)90175-5.

[32] S. Soldini. *Design and Control of Solar Radiation Pressure Assisted Missions in the Sun-Earth Restricted Three-Body Problem*. PhD thesis, UNIVERSITY OF SOUTHAMPTON, 2016.

[33] S. Soldini and S. Colombo, C.and Walker. Comparison of hamiltonian structure-preserving and floquét mode station-keeping for libration-point orbits. 08 2014. doi: 10.2514/6.2014-4118.

[34] M. Stramacchia, C. Colombo, and F. Bernelli-Zazzera. Distant retrograde orbits for space-based near earth objects detection. *Advances in Space Research*, pages 967–988, 2016. doi: http://dx.doi.org/10.1016/j.asr.2016.05.053.

[35] V. Szebehely. *Theory of orbits in the restricted problem of three bodies.* Press Inc., New York., 1967. doi: https://doi.org/10.1016/B978-0-12-395732-0.50007-6.

[36] J. R. Wertz. *spacecraft attitude determination and control.* Kluwer Academic Publishers., 1978.

[37] M. Xin, S. N. Balakrishnan, and H. J. Pernicka. Libration point stationkeeping using the $\theta$-d technique. *stronautical Sciences*, 2008. doi: https://doi.org/10.1007/BF03256550.

[38] G. D. Yàrnoz, J. P. Sànchez, and C. R. McInnes. Easly retrievable obects among the neo population. *Celest Mech Dyn Astr*, pages 367—-388, 2013. doi: https://doi.org/10.1007/s10569-013-9495-6.

[39] E. Zimovan. Characteristics and design strategies for near rectilinera halo orbits within the earth-moon system. Master's thesis, Purdue University, 2017.